J Comput Neurosci (2016) 40:27–50
DOI 10.1007/s10827-015-0582-4

Effects of polarization induced by non-weak electric fields on the excitability of elongated neurons with active dendrites

Robert I. Reznik[1] · Ernest Barreto[1] · Evelyn Sander[2] · Paul So[1]

Received: 25 March 2015 / Revised: 17 October 2015 / Accepted: 22 October 2015 / Published online: 11 November 2015

Abstract An externally-applied electric field can polarize a neuron, especially a neuron with elongated dendrites, and thus modify its excitability. Here we use a computational model to examine, predict, and explain these effects. We use a two-compartment Pinsky-Rinzel model neuron polarized by an electric potential difference imposed between its compartments, and we apply an injected ramp current. We vary three model parameters: the magnitude of the applied potential difference, the extracellular potassium concentration, and the rate of current injection. A study of the Time-To-First-Spike (TTFS) as a function of polarization leads to the identification of three regions of polarization strength that have different effects. In the weak region, the TTFS increases linearly with polarization. In the intermediate region, the TTFS increases either sub- or super-linearly, depending on the current injection rate and the extracellular potassium concentration. In the strong region, the TTFS decreases. Our results in the weak and strong region are consistent with experimental observations, and in the intermediate region, we predict novel effects that depend on experimentally-accessible parameters. We find that active channels in the dendrite play a key role in these effects. Our qualitative results were found to be robust over a wide range of inter-compartment conductances and the ratio of somatic to dendritic membrane areas. In addition, we discuss preliminary results where synaptic inputs replace the ramp injection protocol. The insights and conclusions were found to extend from our polarized PR model to a polarized PR model with I_h dendritic currents. Finally, we discuss the degree to which our results may be generalized.

Keywords Electric fields · Excitability · Hippocampus · Pyramidal neurons

Action Editor: Gaute T. Einevoll

✉ Robert I. Reznik
robert.reznik@cox.net

Ernest Barreto
ebarreto@gmu.edu

Evelyn Sander
esander@gmu.edu

Paul So
paso@gmu.edu

[1] School of Physics, Astronomy, and Computational Sciences and The Krasnow Institute for Advanced Study, George Mason University, Fairfax, VA 22030, USA

[2] Department of Mathematical Sciences, George Mason University, Fairfax, VA 22030, USA

1 Introduction

Neurons, whether in the intact nervous system or in experimental preparations, are commonly subjected to electric fields. These electric fields may be external or endogenous. External sources may be environmental (e.g. power lines, wireless transmissions), or be clinically or experimentally applied. Electric fields are applied to the surface of the brain to affect cortical regions, and probes have been implanted to stimulate sub-cortical regions. Electrical stimuli are currently being used in a number of therapies including those to alleviate depression and the effects of Parkinson's disease. In addition, the search for a viable means of controlling seizures has led to a number of experiments involving

electrical stimuli, both *in vitro* and *in vivo*, as well as human trials (for a review see Han et al. 2014).

Existing therapies using Deep Brain Stimulation (DBS) for Parkinson's disease, depression, and experimental human trials for seizure control use oscillating electric fields. However, there have been some promising experiments where epileptiform activity was suppressed through the application of constant electric fields or constant fields applied in pulses at very low frequencies. These experiments include placing a hippocampal slice between electrodes to establish a DC field (Bikson et al. 2004; Gluckman et al. 1996, 2001; Ghai et al. 2000), and applying a single DC pulse onto a Cs^+ model of epilepsy (Mikkelsen et al. 2013). *In vivo* experiments include polarizing low-frequency electric fields (PLEF) in a rat model of epilepsy (Sunderam et al. 2009; Richardson et al. 2003).

Therapeutic methods that are applied proximally to the scalp and act on the cortex are attractive since they are non-invasive. One such method is Transcranial Direct Current Stimulation (tDCS). Typically tDCS uses two electrodes positioned on top of the head, and current flows from them through the skull, with a fraction of the current reaching the cortex. The electric fields and induced polarization on cortical neurons due to tDCS are estimated to be low, with fields of less than $1 V/m$ and cell membrane polarization less than $1 mV$ (Bikson and Rahman 2013; Miranda et al. 2006).

Endogenous electric fields include those associated with the normal rhythmic activity of populations of neurons (e.g., the theta and gamma rhythms). In the hippocampus, endogenous field strengths range from about 2–70 mV/mm in amplitude (Weiss and Faber 2010). The susceptibility of the somatic transmembrane potential to be polarized has been estimated for both DC and AC fields. The polarization of CA3 pyramidal somata to a DC field has been found to be nearly linear up to, at least, 16 mV/mm, yielding a constant susceptibility or polarization length of 0.18 mm. Deans et al. (2007) and Radman et al. (2007, 2009) have measured hippocampal and cortical pyramidal neurons and found their polarization lengths to be between about 0.1 mm and 0.5 mm, and most frequently near 0.2 mm. For AC fields, the susceptibility is frequency dependent with higher frequencies being less polarizing as the neuron acts as a low-pass filter. At 10 Hz, the polarization length is about 0.225 mm, and at 100 Hz it is 0.05 mm (Deans et al. 2007). In addition, near constant uniform fields have been detected up to 7.5 mV/mm and associated with changes in the potassium concentration that emerge along with neural hyperactivity (Dietzel et al. 1989).

Despite its importance, our understanding of how electric fields interact with and affect the functioning of neural populations remains incomplete. An understanding of such phenomena and their potential medical implications requires a careful analysis of effects on both single neurons and populations due to electric fields with a range of amplitudes, frequencies, and waveforms. Here we focus on the simplest case of a single neuron subject to a constant uniform field. This study serves as a step towards understanding the excitability of elongated neurons with active dendrites subject to electric fields. The results here may be relevant to *in vivo* and *in vitro* work involving DC fields.

In response to a uniform electric field, charge within a cell spreads out along the field lines until an obstruction such as a cell wall is encountered. The resulting charge distribution creates polarization within the neuron. Here, when we speak of polarization, we are referring to the shift in membrane potential due to imposed differences in the extracellular potential along the neuron. The sensitivity of neurons, particularly elongated pyramidal neurons, to even low amplitude electric fields has been shown experimentally (Francis et al. 2003). Computational models of polarization and its effects on single neurons have ranged from a detailed finite-element model (Pucihar et al. 2009) to single-compartment models (Berzhanskaya et al. 2007; Reato et al. 2010). Another approach has employed multi-compartment models with an electric potential applied across the compartments. These compartment models have varied in complexity from two-compartment models (Gluckman et al. 1998; Park et al. 2003, 2005) to a 19-compartment model (Traub et al. 1985a, b). Several studies, including this one, use the model of Pinsky and Rinzel (1994), which is itself a simplified version of the 19-compartment model of Traub et al. (1991). Recently a bifurcation study of neural excitability in response to polarization has been applied to a two-compartment modified Morris-Lecar model with passive dendrites (Yi et al. 2014).

Experiments (Bikson et al. 2004; Radman et al. 2007, 2009) have shown that as long as the polarization is not too great, the somatic transmembrane potential of pyramidal neurons at rest is linearly proportional to the degree of polarization. In addition, changes in spike timing in response to an injected ramp current were found to vary linearly with polarization in the range studied, which was 3–5 mV. These results could be explained by a simple leaky (*i.e.* passive conductance) integrate-and-fire model. Accordingly, we define the weak polarization region as those values of polarization for which the neuron behaves passively, i.e., the membrane conductances remain constant. Systematic measurements of the size of this linear response region are lacking, as they have not been the focus of previously published work.

The emphasis on smaller electric fields is understandable. Many medical applications seek the least invasive methods. Also, endogenous field effects such as the gamma and theta oscillation in the hippocampus are often only

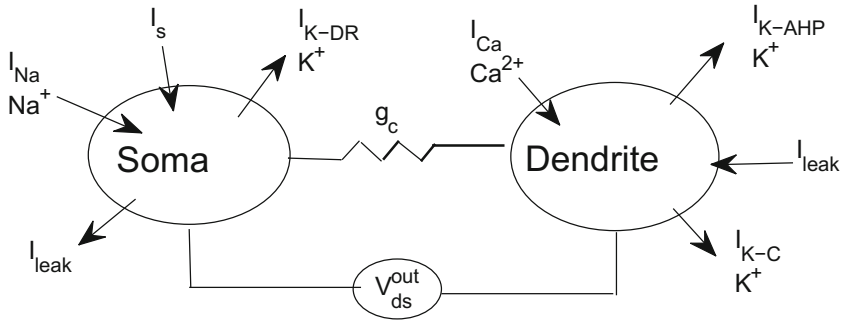

Fig. 1 Two-compartment Pinsky-Rinzel model neuron with electric field. Arrows denote the direction of the currents during stimulation from rest. Differences in potential along the body of a neuron outside the neural membrane induces a polarization within the neuron. Polarization induces a current between the two model compartments. All the active currents in the model involve cations so inward arrows are depolarizing and outward hyperpolarizing. Active currents in the soma are the depolarizing sodium (Na) and the hyperpolarizing potassium-delayed rectifier (K-DR). In the dendrite the calcium (Ca) current is depolarizing while the potassium after-hyperpolarization and potassium-calcium (K-C) are hyperpolarizing. I_s and I_d include any constant baseline currents as well as any stimulating currents

several millivolts in amplitude (Csicsvari et al. 2003) and thus probably within the passive region. We may estimate, however, that there exist some instances for which a neuron might experience polarization outside the passive region. As mentioned above, the polarization length of pyramidal neurons in a uniform field has been measured between 0.1 mm and 0.5 mm. Experiments on hippocampal slices have used field strengths exceeding 100 mV/mm (Bikson et al. 2004; Richardson et al. 2005) implying that pyramidal neurons may have experienced polarizations in excess of 50 mV. Very low frequency pulses were applied to the Rat hippocampus yielding an estimated 16–20 mV/mm electric field (Sunderam et al. 2009). For moderate to high polarization lengths, such a field would induce a polarization outside of the weak region. The polarization of a pyramidal neuron in the hippocampus due to oscillating endogenous fields is harder to estimate. As noted above, the polarization decreases with increasing frequency and the largest amplitude endogenous fields, sharp waves, and epileptic discharges are associated with higher frequencies ($>$ 50 Hz). To exceed the outer limit of the weak polarization region, 5 mV, at the maximum estimated endogenous field amplitude of 70 mV/mm, a sensitivity of at least 0.07 mm is required. The 0.07 mm is, in fact, what was measured for a CA3 pyramidal cell at 50 Hz (Deans et al. 2007).

In this study, we explore the effects and underlying mechanisms over a broader range of polarizations, with emphasis

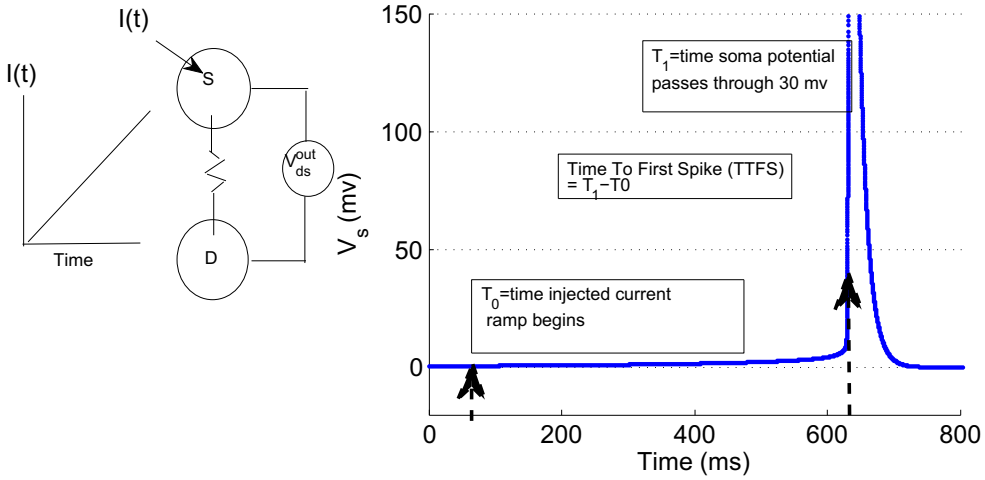

Fig. 2 Summary schematic of computational protocols used to characterize how polarization affects excitability. $I_{s,inj}(t)$ is the ramp current injected into the soma and is equal to $\overline{I_s} + M(t - t_0)$ where M is in $\mu A/(cm^2 sec)$. The Time To First Spike (TTFS) is defined as the time it takes for the model neuron's somatic membrane potential to pass through a predefined threshold value. This paper will be concerned only with the dynamics driving the polarized neuron from rest to first spike. The TTFS was insensitive to soma potential thresholds above 10 mV

on the effects beyond the weak polarization regime. We use the model of Pinsky and Rinzel (1994) and modify it to allow for an imposed extracellular potential difference between the two compartments. Polarization is then parametrized by this potential difference. With this model we study how polarization affects excitability and how changes in the extracellular potassium concentration and the rate of stimulating current injection modifies these effects. We chose the Pinsky-Rinzel (PR) model because it has the minimum number of compartments (two) needed to explore the effects of polarization on a neuron with distinct and spatially segregated ion channels. Furthermore, the PR model uses experimentally-derived ion channel kinetics to model specific currents, allowing for a more physiological interpretation compared to simplified lower-dimensional models.

In Section 2 (Models and Methods) we derive the polarized PR model, present our stimulation protocol, define the time-to-first spike (TTFS), and discuss our numerical methods. In Section 3 (Results) we present curves of TTFS as a function of polarization for different injection rates and extracellular potassium concentrations. We perform our computations over a range of inter-compartmental conductances and ratios of somatic to dendritic membrane surface area. These results are first computed using a commonly-used current injection protocol that might be amenable to experiment. To examine a more biologically plausible model, we subject the polarized model neuron to synaptic (AMPA) excitation. Lastly, we see how our results change when we introduce I_h currents into the dendritic compartment. In Section 4 (Discussion), we summarize our results and consider how they might be generalized to biological neurons.

2 Models and methods

2.1 Polarizable pinsky-rinzel model: approach and computational methods

In the PR model, the primary ionic mechanisms for depolarization are the sodium ion channels of the soma and the calcium channels of the dendrite. Hyperpolarizing currents are provided by the I_{K-AHP} and I_{K-C} in the dendrite

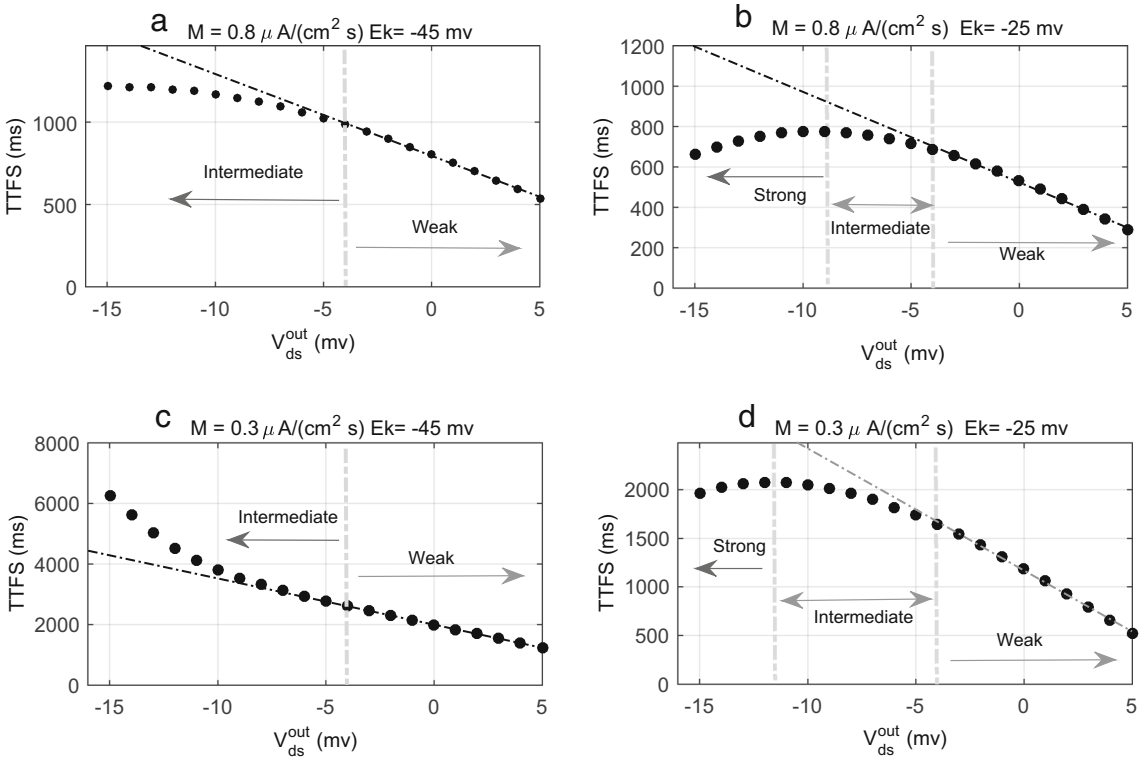

Fig. 3 For decreasing values of V_{ds}^{out}, the TTFS increases linearly until about $-4\,mV$. As V_{ds}^{out} continues to decrease below this value, the TTFS curves display either sublinear (**a**, **b**, **d**) or superlinear (**c**) behavior depending on the rate of current injection (M) and the potassium reversal potential E_K. Here, as for all the computations in this paper, $\overline{I_s} = -0.5\ \mu A/cm^2$. The weak, intermediate, and strong, polarization regions are labeled

and I_{K-DR} in the soma. Current between the somatic and dendritic compartments flow passively in proportion to the potential difference. The somatic and dendritic membrane potentials, the calcium level in the dendrite, four voltage-dependent gates, and one calcium-dependent gate constitute a system of eight coupled ordinary differential equations. In this paper, we focus on the effects that polarization *induced* by electric fields have on a neuron's dynamics. The source for the electric field, how it couples into the extracellular medium and how charge redistributes itself around the neural membrane will not be considered (for details into field calculations see for example (Holt and Koch 1999; Tranchina and Nicholson 1986; Vigmond et al. 1997). The component of the electric field relevant to the neural dynamics is along the soma-dendrite axis and is modeled by the outside potential difference between the soma and the dendrite, V_{ds}^{out}. The polarization is then parameterized by V_{ds}^{out}.

We modify the PR model to accommodate this polarization between compartments as was done in Gluckman et al. (1998) and Park et al. (2003, 2005). The transmembrane potential is defined by the difference in potential across the cell membrane.

$$V_s = V_s^{in} - V_s^{out} \tag{1a}$$

$$V_d = V_d^{in} - V_d^{out} \tag{1b}$$

Membrane channels are functions of the transmembrane potentials. However, current flowing passively between the two compartments is proportional to the difference in

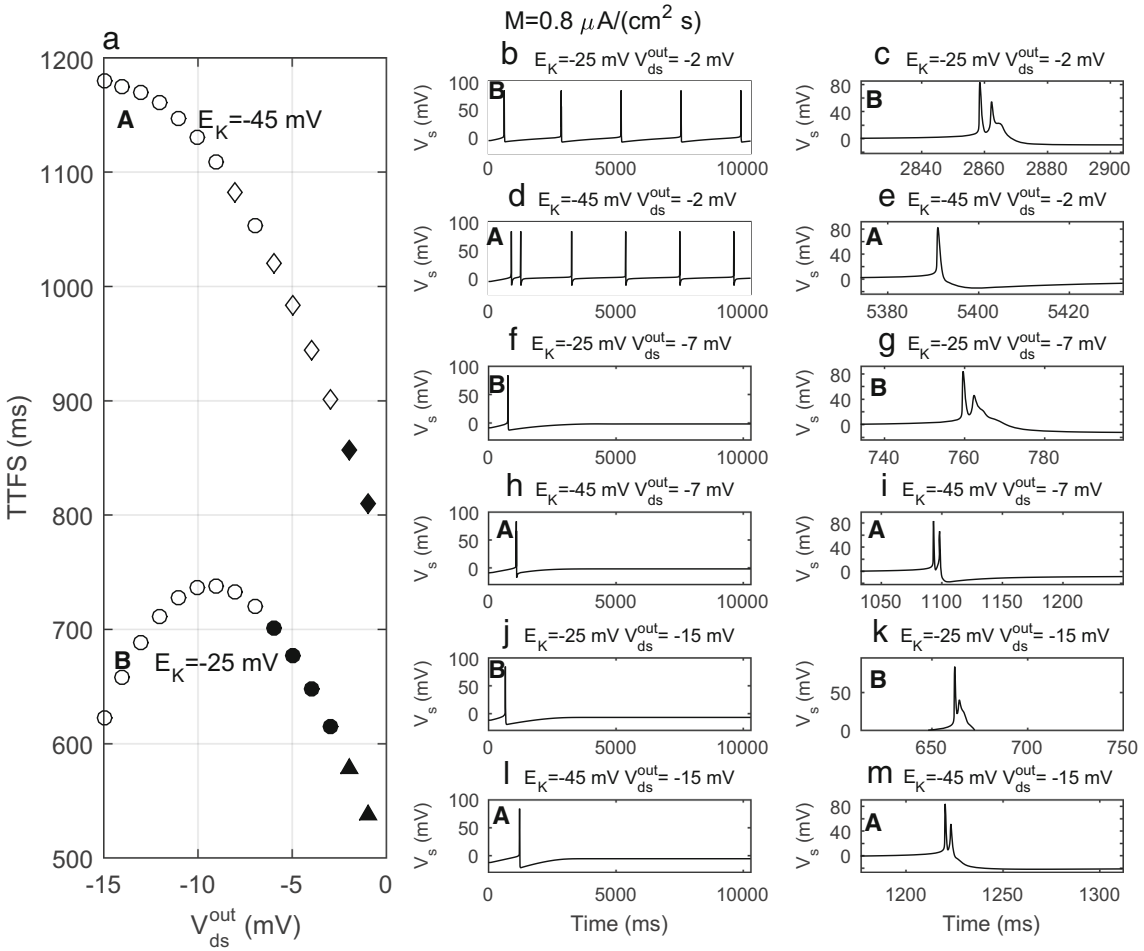

Fig. 4 Spike behavior for two sublinear profiles, A and B. For both profiles $M = 0.8\,\mu A/(cm^2 s)$. $E_K = -45$ mV for A and $EK = -25$ mV for B. All parameter values are the same as that used in Fig. 3a and b. Here, however, the integration is continued past the TTFS with a constant current injection $= M \cdot TTFS$. Filled symbols denote periodic spiking or busting, and open symbols denote an isolated spike or burst, or that activity was at such a low frequency that no other spikes appeared during the 10 second run-time. Shapes symbolize number of spikes within a particular waveform ($< 20ms$): diamond denotes a single spike, circle denotes a spike doublet, and triangle denotes 3 or more spikes (e.g. a burst). The third column of plots is a magnification around a spike in the second column of plots

their intracellular potentials, V_s^{in} and V_d^{in}. The original PR model, as in most models, implicitly assumed a constant extracellular potential, $V_s^{out} = V_d^{out}$. In this case, the intracellular potential between compartments, $(V_d^{in} - V_s^{in})$, is equal to the difference in transmembrane potentials, $(V_d - V_s)$.

Allowing for our compartments to have two different extracellular potentials, we define the potential difference directly outside the dendrite and soma as $V_{ds}^{out} \equiv V_d^{out} - V_s^{out}$. With the inter-compartment conductance given by g_c and ρ defined as the fraction of somatic surface area to the total cell surface area, the current out of the dendrite and into the soma is defined as I_{ds}^{in} and is given by:

$$I_{ds}^{in} = \frac{g_c}{\rho}\left(V_d^{in} - V_s^{in}\right) = \frac{g_c}{\rho}\left(V_d - V_s + V_{ds}^{out}\right). \tag{2}$$

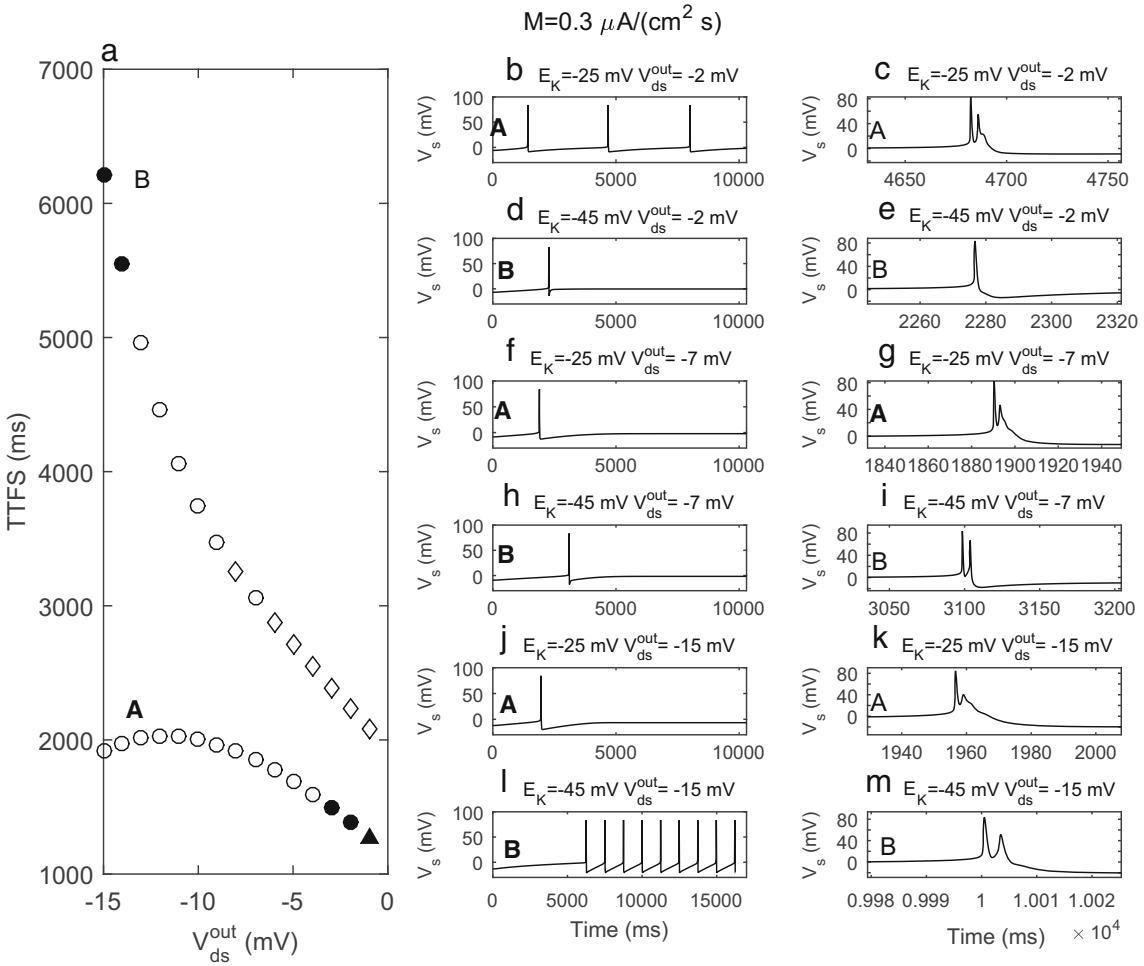

Fig. 5 Spike behavior for a sublinear profile, A, and superlinear profile, B. Both profiles use a slow injection rate, $M = 0.3\mu A/(cm^2 s)$. For profile A $E_K = -25$ mV and for profile B $E_K = -45$ mV. All parameter values are the same as that used in Fig. 3a and b. Here, however, the integration is continued past the TTFS with a constant current injection $= M \cdot TTFS$. Filled symbols denote periodic spiking or busting while open symbols are isolated spike or bursts or, at least, with a period greater than 10 s. Shapes symbolize number of spikes within a particular waveform ($< 20\,ms$): diamond denotes a single spike, circle denotes a spike doublet, and triangle denotes 3 or more spikes (e.g. a burst). The third column of plots is a magnification around a spike in the second column of plots. Notice how the superlinear profile exhibits isolated spikes at weak polarizations and periodic spiking near the end of the intermediate region. While the sublinear profile exhibits periodic spiking/bursting at weak polarizations and isolated spikes in the intermediate region. Superlinear and sublinear profiles show qualitative differences in both spike behavior and TTFS (see Fig. 6)

The polarized PR model follows,

$$\begin{aligned} C_m \cdot dV_s/dt &= I_{sLeak}(V_s) + I_{Na}(V_s, h) \\ &\quad + I_{K-DR}(V_s, n) + I_{ds}^{in} + I_{s,inj}(t), \qquad (3a) \\ C_m \cdot dV_d/dt &= I_{dLeak}(V_d) + I_{Ca}(V_d, s) \qquad (3b) \\ &\quad + I_{K-AHP}(V_d, q) + I_{K-C}(V_d, Ca, c) \\ &\quad - I_{ds}^{in} \frac{\rho}{1-\rho} \\ dCa/dt &= -0.13 I_{Ca} - 0.075 Ca \qquad (3c) \end{aligned}$$

Ca represents a unitless measure of the amount of intracellular calcium, Ca^{2+}. In the equation governing intracellular calcium levels, the coefficient -0.075 is based on optical measurements of the decay of calcium in Purkinje dendrites ($-0.075 s^{-1} = 1/\tau_{Ca} = 1/13.33\ ms$) (Traub et al. 1991; Traub and Milesm 1991). The sign of the coefficient -0.13 multiplying I_{Ca} means that current into the dendritic compartment results in an increase in intracellular calcium (Traub et al. 1991)[1] The only difference between the polarized PR model and the original one is the addition of the terms I_{ds}^{in} and $-I_{ds}^{in}\rho/(1-\rho)$ in the equations for the somatic and dendritic compartments, respectively. Note that since we define ρ as the fraction of somatic surface area to total surface area, I_{ds}^{in} is then defined as current per total soma area. In this paper, as in the original PR model and the models used in the Park et al. papers referenced above, we shall assume that the somatic and dendritic compartment surface areas are equal, so that $\rho = 0.5$ and the flow of current from the soma to the dendrite is $-I_{ds}^{in}$. The individual currents with their dependencies on the dynamic gating variables h, n, s, c, and q follow.

$$\begin{aligned} I_{sLeak} &= -g_L (V_s - E_L) \qquad (4) \\ I_{dLeak} &= -g_L (V_d - E_L) \\ I_{Na} &= -g_{Na} m_\infty^2 h (V_s - E_{Na}) \\ I_{K-DR} &= -g_{K-DR} n (V_s - E_k) \\ I_{Ca} &= -g_{Ca} s^2 (V_d - E_{Ca}) \\ I_{K-AHP} &= -g_{K-AHP} q (V_d - E_k) \\ I_{K-C} &= -g_{K-C} c \chi (V_d - E_k) \end{aligned}$$

These currents and whether they flow inward (depolarizing) or outward (hyperpolarizing) at typical steady-state values are depicted by arrows in Fig. 1. Note that for our model, a cathode is imagined to be placed near the soma and the anode near the apical dendrites, so that a positive (negative) field depolarizes (hyperpolarizes) the soma and hyperpolarizes (depolarizes) the dendrite. Note that this convention is a reversal in field sign from that found in Bikson et al. (2004), Radman et al. (2007, 2009), and (Berzhanskaya et al. 2007), but follows that used in Park et al. (2003, 2005). There are five gating variables (h, n, s, c, and q) whose kinetics take on the standard Hodgkin-Huxley form. The gating variables h and n are functions of V_s, s and c are functions of V_d, and both q and χ are functions of the intracellular calcium concentration Ca. Equations (3) and (4) are thus coupled with the five first-order gating kinetics given below:

$$dh/dt = (h_\infty(V_s) - h)/\tau_h(V_s) \qquad (5a)$$

$$dn/dt = (n_\infty(V_s) - n)/\tau_n(V_s) \qquad (5b)$$

$$ds/dt = (s_\infty(V_d) - s)/\tau_s(V_d) \qquad (5c)$$

$$dc/dt = (c_\infty(V_d) - c)/\tau_c(V_d) \qquad (5d)$$

$$dq/dt = (q_\infty(Ca) - q)/\tau_q(Ca). \qquad (5e)$$

For our model, the stimulus is a ramp current, I_{ramp}, injected into the soma. The term $I_{s,inj}$ in Eq. (3) is the sum

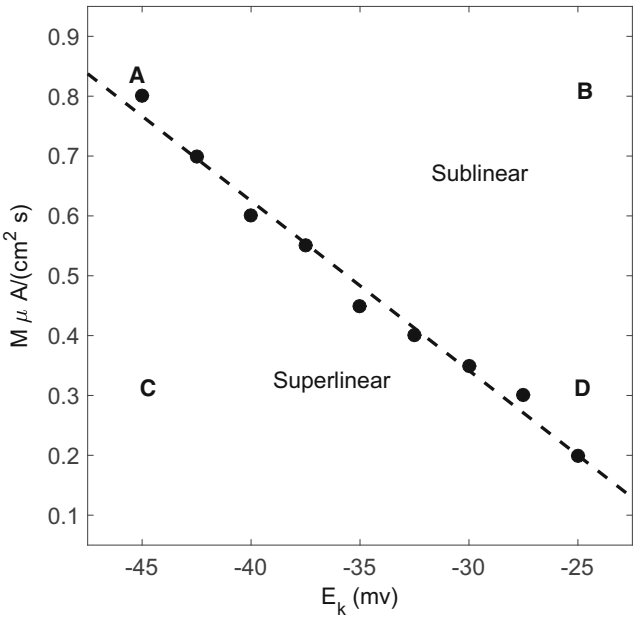

Fig. 6 The $E_K - M$ parameter-space boundary that separates sub- and super-linear behavior exhibits an inverse relationship. Below the line the profile is superlinear and above it is sublinear. As discussed in Section 2.2.2 sublinear and superlinear profiles were associated with the sign of the numerical second-derivative computed over the intermediate polarization region, $V_{ds}^{out} \in [-15\,mV, -4\,mV]$. Parameter values are as in Fig. 3

[1] Traub et al. (1991) presents an abstract model of intracellular calcium where each compartment's rate of absorption can be varied by varying the thickness of an imagined sub-cellular membrane. This coefficient was fine-tuned to best match experimental data.

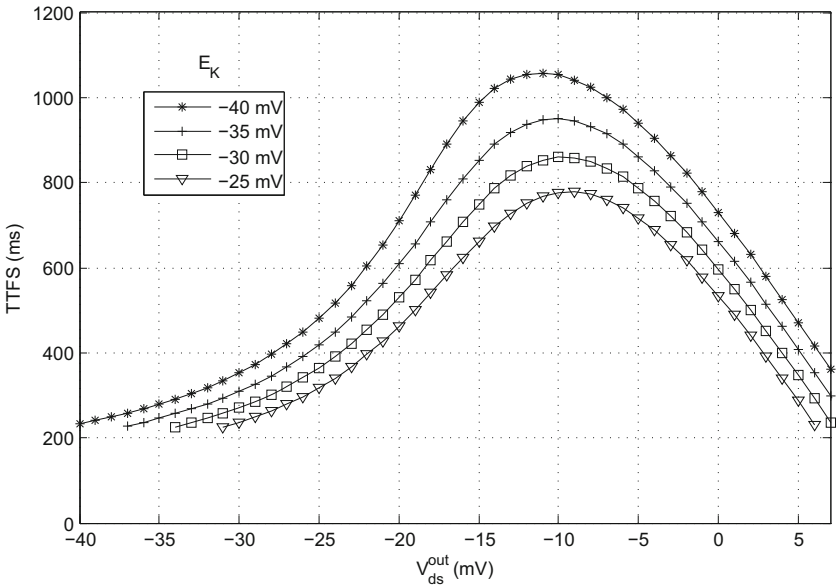

Fig. 7 The strong polarization region begins where the TTFS starts to decrease as V_{ds}^{out} decreases. Here the TTFS values are calculated for a fast injection rate ($M = 0.8\mu A/(cm^2 s)$) at four different E_K

of the ramp current and a constant bias current, $\overline{I_s}$. For the computations reported here, $\overline{I_s} = -0.5\mu A/cm^2$, which was used as the standard value in the original PR model.

$$I_{s,inj}(t) = \overline{I_s} + I_{ramp}(t) \tag{6}$$

where I_{ramp} is defined as the following linearly increasing function with ramp rate M.

$$I_{ramp}(t) = M(t - t_0). \tag{7}$$

The ramp protocol, illustrated in Fig. 2, calls for the current density to be steadily increased until the soma is depolarized to 30 mV. Note that in Traub's 19-compartment model and the PR model, the potentials are normalized such that the resting potential of the unpolarized neuron is 0 mV. In our numerical experiments, we estimate the TTFS as the time when the somatic membrane potential reaches 30 mV. The metric TTFS is used since it is relevant to excitable but resting neurons, and pyramidal neurons are typically associated with such states.

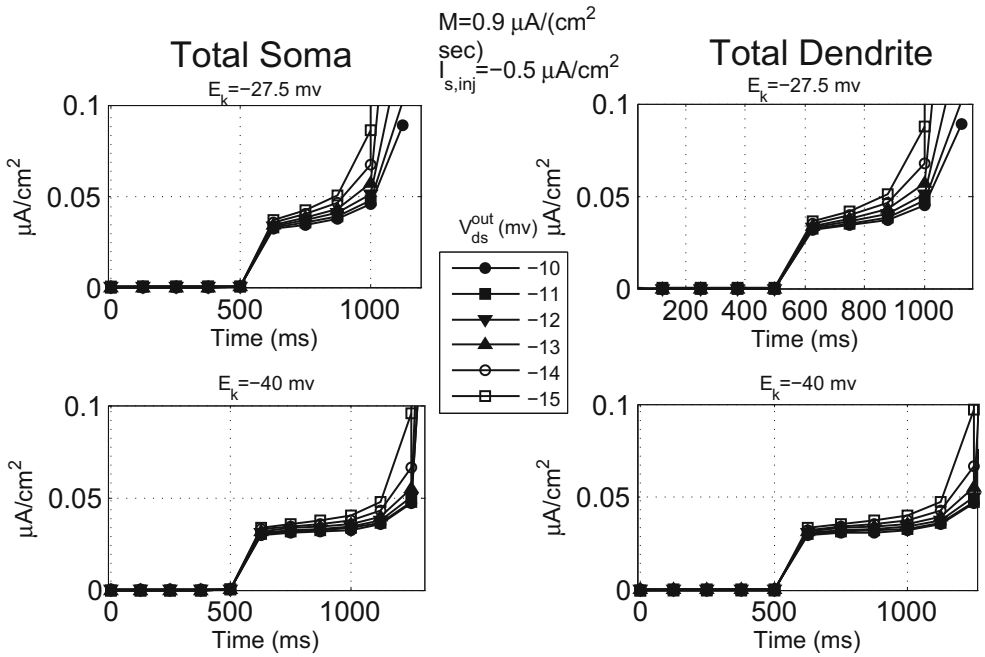

Fig. 8 Here we plot the total somatic and dendritic currents, the right-hand sides of dV_s/dt and dV_d/dt. Even at the fastest injection rates the somatic and dendritic potentials change at the same rate. This holds true during the soma injected current for all E_K, M, and V_{ds}^{out} we examined

We adopt the numerical values for the reversal potentials and conductances as given in the original PR model:

$$\begin{aligned} E_{Na} &= 120 \text{ mV}, E_L = 0 \text{ mV} \\ E_{Ca} &= 140 \text{ mV}, C_m = 3 \text{ uf/cm}^2 \\ g_L &= 0.1 \text{ mS/cm}^2, g_{Na} = 30 \text{ mS/cm}^2 \\ g_{K-DR} &= 15 \text{ mS/cm}^2, g_{K-AHP} = 0.8 \text{ mS/cm}^2 \\ g_{K-C} &= 15 \text{ mS/cm}^2, g_{Ca} = 10 \text{ mS/cm}^2 \\ g_c &= 2.1 \text{ mS/cm}^2, \rho = 0.5, \overline{I_s} = -0.5\mu A/cm^2 \end{aligned} \tag{8}$$

The extracellular potassium concentration, $[K^+]_o$, controls the reversal potentials of the somatic hyperpolarizing potassium-delayed rectifier current I_{K-DR}, the dendrite-hyperpolarizing calcium-activated potassium current I_{K-C}, and the after-hyperpolarizing potassium current I_{K-AHP}. Extracellular potassium levels are known to increase with increased neuronal activity (Moody et al. 1974), and the increasing extracellular potassium in turn excites the surrounding neurons. However, the positive feedback between neural hyper-activity and extracellular potassium is modulated by Glia cells which tend to suppress high extracellular potassium through uptake and spatial buffering. For more on the dynamics of the ion concentrations and its effects on neuronal behavior see Cressman et al. (2009, 2011), Barreto and Cressman (2011). E_K in the polarized PR model is related to the extracellular potassium concentration through the Nernst equation. Since the extracellular potassium is known to vary *in vivo* and can be manipulated in the laboratory we examined the excitability of the polarized PR model over a range of physiologically plausible E_K and corresponding extracellular potassium concentrations. The higher the extracellular potassium concentration the higher the reversal potential. Here we varied E_K from $-25\,mV$ to $-45\ mV$. To place these values in context note that a reversal potential of $E_K = -38.56\ mV$ has been associated with a normal potassium environment (Park et al. 2005) corresponding to $[K^+]_o = 3.5\,mM$ assuming $[K^+]_i = 140\,mM$ and $T = 36.9\,^\circ C$. A high extracellular potassium concentration is $[K^+]_o = 8.45\,mM$ corresponding to $E_K = -15\,mV$ and is associated with spontaneous periodic bursting. Such high potassium levels have been measured in hippocampal slices exhibiting epileptic like activity (McNamara 1994) and *in vivo* in seizing cats (Moody et al. 1974).

In Section 3.6 we replace the ramp current stimulus with synaptic AMPA input modeled as in Pinsky and Rinzel (1994) and Park et al. (2003, 2005). This class of model for synaptic conductance assumes that the transmitter release is always at a maximum as long as the pre-synaptic potential $V_{s,pre}$ exceeds a certain threshold potential. The equation for the AMPA synaptic conductance is as follows:

$$\begin{aligned} I_{AMPA} &= \overline{g}_{AMPA} W(t)(V_d - V_{syn}) \\ W' &= H(V_{s,pre} - 20) - W/2, \end{aligned} \tag{9}$$

where H denotes the Heaviside function. We apply the AMPA current by defining $V_{s,pre}$ as follows:

$$\begin{aligned} V_{s,pre} &= AH(t - t_i)H(t_i + t_{spkdur} - t) \\ t_{spkdur} &= 1.2\ ms \\ A &> 20\ mV \end{aligned} \tag{10}$$

in Section 3.7, we include a model of the I_h current into our polarized PR model. We model I_h as in Lippert and Booth (2009) and Golding (2005). The family of I_h currents have

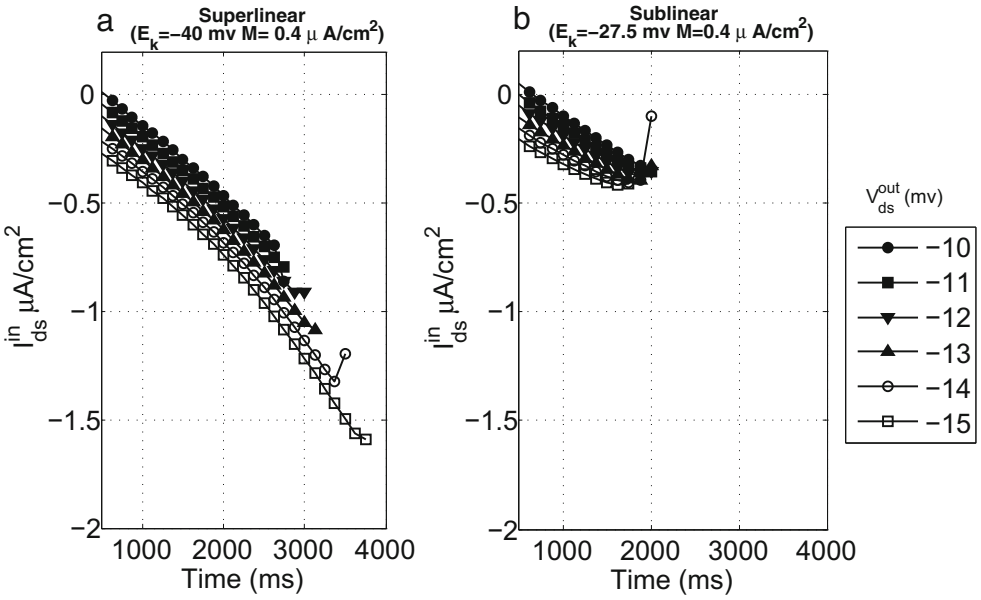

Fig. 9 Soma shunting to dendrite. $M = 0.4\mu A/cm^2$. I_{ds}^{in} is defined to be the current out of the dendrite and into the soma. Thus, negative values of I_{ds}^{in} indicate that this current flows from the soma to the dendrite. The curves terminate when a somatic membrane potential spike occurs. Compared to the sublinear case the superlinear shunting is increased by approximately 20 percent. This increase in shunting is enough to not only delay a somatic spike, but to cause significant increase in dendritic outward current. For the case shown, the TTFS increases by approximately 30 % for $V_{ds}^{out} = -10$ mV to a factor of two for $V_{ds}^{out} = -15$ mV

a unique set of characteristics including an inward current activated at hyperpolarized membrane potentials, significant current at rest, moderately long time constants, and various regulated states characterized by changes in channel density and activation potentials. Here, we use i to denote the I_h gating variable. The model is

$$I_h = g_h i(V_d - E_h) \tag{11a}$$
$$di/dt = (i_\infty(V_d) - i)/\tau_i(V_d) \tag{11b}$$
$$i_\infty = \frac{a_i(V_d)}{a_i(V_d) + b_i(V_d)} \tag{11c}$$
$$\tau_i = \frac{500}{a_i(V_d) + b_i(V_d)} \tag{11d}$$
$$a_i\,(V_d) = exp\left(0.1054\left(V_d - V_{i-half}\right)\right) \tag{11e}$$
$$b_i\,(V_d) = exp\left(0.1581\left(V_d - V_{i-half}\right)\right) \tag{11f}$$

a and b determine the steady-state value, i_∞, τ_i is the time constant, and V_{i-half} is the half-activation parameter. Also as in Lippert and Booth (2009) we adopted four pairs of g_h and V_{i-half} parameter values representing a control state ($0.03\ mS/cm^2$, $-21\,mV$), a low level of I_h up-regulation ($0.035\,mS/cm^2$, $-18\,mV$) and a high level of up-regulation ($0.04\ mS/cm^2$, $-15\,mV$) in accordance with serotonergic modulation of I_h (Gasparini and DiFrancesco 1999). To this we also added the most highly-regulated state looked at by Lippert and Booth (2009) ($0.06\,mS/cm^2$, -11 mV). Here, as before the reversal potentials are normalized to correspond with a resting potential of 0 mV for the unpolarized neuron.

2.2 Numerical methods

2.2.1 Computing the TTFS

When performing calculations on excitability, we used only those polarizations for which a stable resting equilibrium exists. The polarized Pinsky-Rinzel neuron was coded in MATLAB. MATLAB's ODE23 was used for integrating the eight-dimensional coupled nonlinear ODE of Eqs. (3–7) with the parameter set given in Eq. (8). For a given choice of E_K and M, a TTFS profile was generated over a range of V_{ds}^{out} for which the model neuron was stable prior to any injected current. The range of V_{ds}^{out} for which the resting equilibrium is stable varied with E_K, but was found to be continuous and generally ranged from around $+15\,mV$ to $-30\ mV$. Stability was first calculated using a nonlinear root-finding method after setting the gating variables

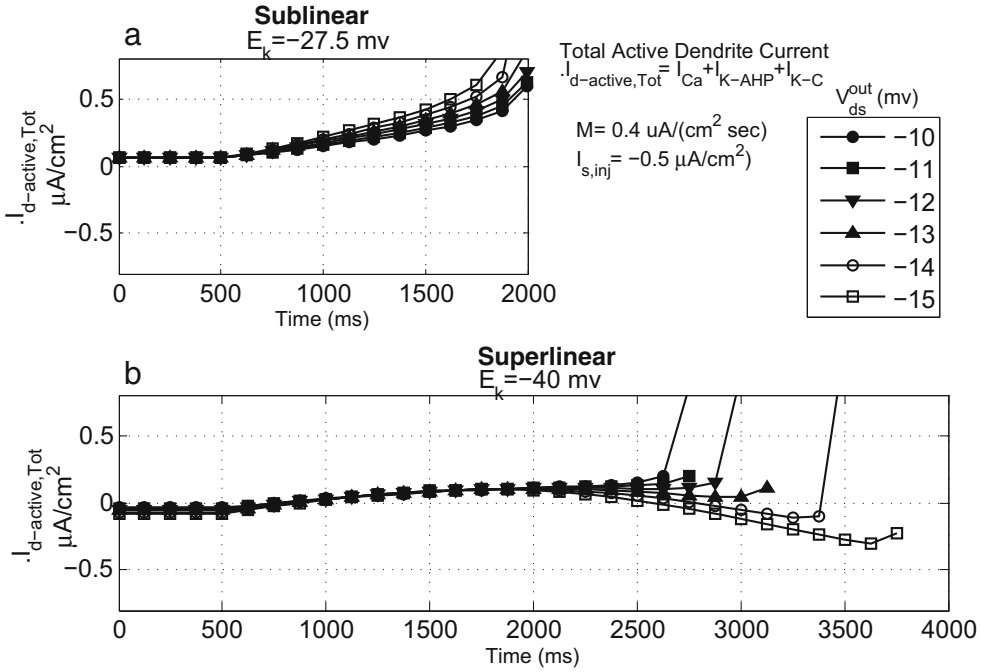

Fig. 10 The active dendritic currents for sublinear and superlinear profiles. Here $M = 0.4\,\mu A/cm^2 s)$ and $I_{s,inj} = -0.5\,\mu A/cm^2$. In (**a**) $E_K = -27.5$ mV and the profile is sublinear. In (**b**) $E_K = -40$ mV and profile is superlinear. The total active dendritic currents are plotted and are equal to the sum of the hyperpolarizing potassium currents, K-AHP and K-C, as well as the depolarizing calcium. $I_{d,active} = I_{K-AHP} + I_{K-C} + I_{Ca}$. For the sublinear profile the total active dendritic currents are monotonic in time and for increasingly negative V_{ds}^{out}. For the superlinear profile with it's stronger hyperpolarizing currents the total active dendrite currents become non-monotonic with time for polarization below around -12 mV. Furthermore for polarizations below around -13 mV the total active dendritic currents become net hperpolarizing

and Ca to their equilibrium values. As a further measure to insure stability, the solutions were integrated for 50 ms prior to the start of ramp injection. To estimate the sensitivity to numerical methods, MATLAB's higher order ODE45 was used in the integration and these were shown to yield TTFS values that differed less than 10^{-9} from those of the faster ODE23. We define a single run of our system to be the computation of the TTFS for a particular V_{ds}^{out}, E_K and M.

2.2.2 Numerical analysis of TTFS profiles

In the intermediate polarization region, it was observed that either the TTFS grew sublinearly or superlinearly with V_{ds}^{out} depending on E_K and M. To quantify the curvature found in the resulting TTFS profiles with respect to the imposed V_{ds}^{out}, we computed a second-order centered difference using the TTFS data points. These were calculated at every V_{ds}^{out}. It was observed that within the intermediate polarization region, $V_{ds}^{out} \in [-4\ mV, -15\ mV]$, the numerically-calculated second derivatives did not change sign as we varied V_{ds}^{out}. This means that for a particular E_K and M, the solution remained either sublinear or superlinear over the intermediate polarization, thus allowing us to unambiguously define a sublinear and superlinear profile by the sign of the second derivative at any of the intermediate polarizations. To bound the values for M at a given E_K at which the profile transitioned between sublinear and superlinear, we increased M starting at the very slow injection rate of 0.05 $\mu\ A/(cm^2 s)$. At this value, the second derivative was always found to be negative, indicating a superlinear profile. As M increased, we determined when the second derivative became positive. The second derivative was computed at 0.25 mV steps over the intermediate polarization and over a grid of E_K and M values. E_K was varied from $-20\,mV$ to $-45\,mV$ in steps of 2.5 mV, while M varied from 0.1 $\mu A/(cm^2 sec)$ to 0.8 $\mu A/(cm^2 sec)$ in steps of 0.05 $\mu A/(cm^2 sec)$. For each E_K, the lowest M value for which the second derivative of the profile became positive was used to estimate the boundary curve separating sublinear and superlinear profiles. Sensitivity to step size was evaluated by performing the same algorithm but for a much smaller step size of 0.075 mV. The smaller step sizes

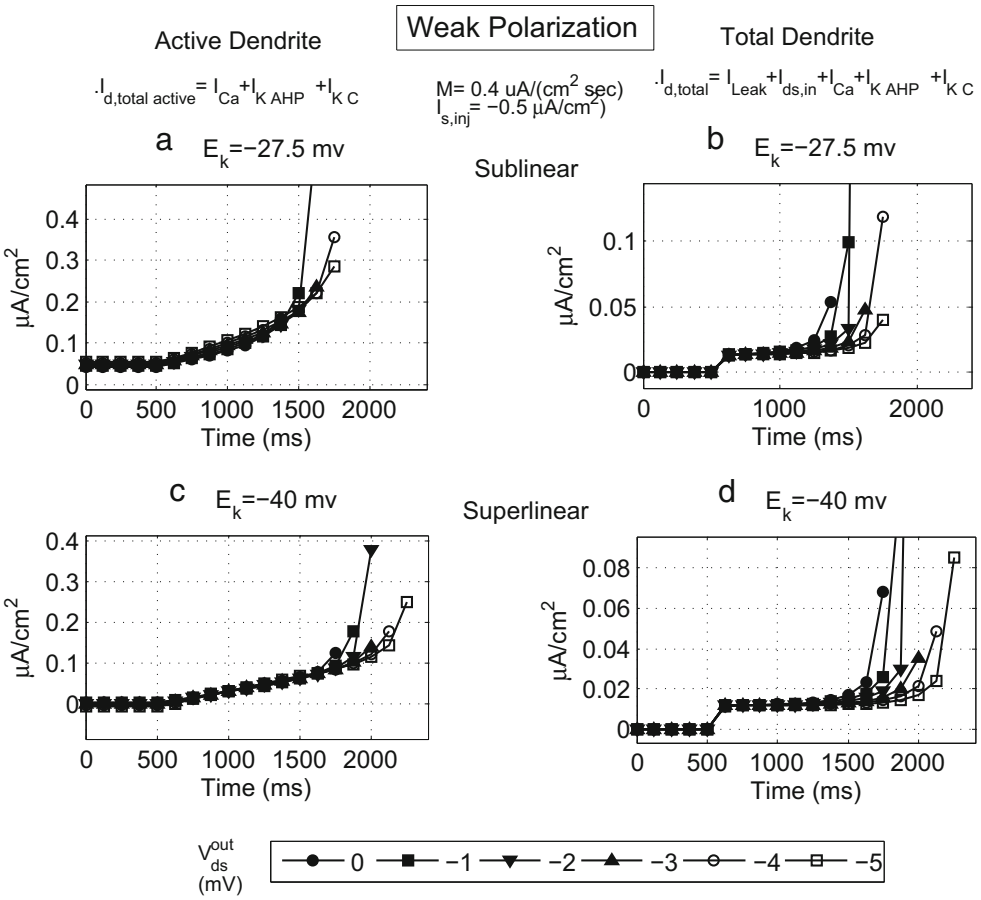

Fig. 11 Plots of the active dendritic membrane currents (*left*), and for comparison, the total dendritic membrane current (*right*). The parameters are the same as in Fig. 10

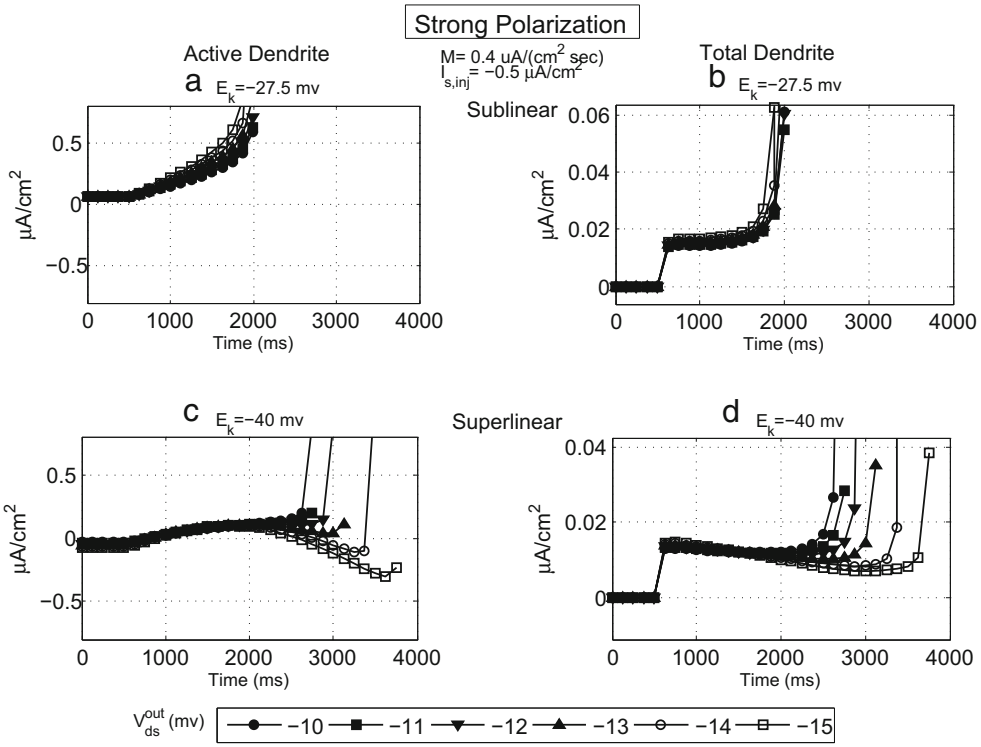

Fig. 12 The superlinear and sublinear profiles emerge only at stronger polarizations which primes the activation of the dendritic channels. For the same parameters as in Fig. 11 but at weak polarizations while there is some increase in the hyperpolarization and longer TTFS there is no qualitative difference in the currents as there is when it is at stronger negative polarizations

resulted in small changes in the second derivative and did not qualitatively change the boundary curve in the $E_K - M$ parameter space.

Code for computations, analysis, and graphics were written in MATLAB and are available online at ModelDB (http://senselab.med.yale.edu/modeldb/).

3 Results

3.1 TTFS profiles

Figure 3 shows four plots of TTFS as a function of V_{ds}^{out}. Each data point on the plot is obtained by integrating Eqs. (3–7) (see Methods) with parameters as in Eq. (8) for the specific values of V_{ds}^{out}, M, and E_k indicated in the figure, and measuring the time until V_s exceeds 30 mV. Each of the plots is obtained using either a high ($-25\,mV$) or low ($-45\,mV$) E_k, and a slow ($0.3\ \mu A/(cm^2 s)$) or fast ($0.8\ \mu A/(cm^2 s)$) current injection rate M. In each case there is a range of polarization for which the TTFS is linear with V_{ds}^{out}, and a range at stronger soma-hyperpolarizing fields for which the TTFS is no longer linear with polarization. We call the linear range the weak polarization region. We define the extent of the weak polarization region by noting the most negative polarization for which the R^2 measure[2] stays above 0.99. In all four cases the TTFS profile deviates from our R^2 criterion at $V_{ds}^{out} = -4\ mV$, which is consistent with experimental observation (i.e., departure from linearity between $-3\ mV$ and $-5\ mV$; see Introduction). Outside the weak polarization region, we see in Fig. 3 that both E_k and M affect how TTFS varies with polarization. For $E_k = -45\ mV$, the fast current injection rate yields a sublinear TTFS profile (Fig. 3a), while the slower ramp injection yields a superlinear one (Fig. 3c). For $E_k = -25\ mV$, the profile is sublinear for both injection rates (Fig. 3b and d).

In Figs. 4 and 5 we show the behavior of the transmembrane potential of the soma versus time, where we continue to integrate our model past the occurrence of the first spike, maintaining a constant current injection at the soma equal to the ramp current at the time of the first spike. Results are shown in Fig. 4 for $M = 0.3\,\mu A/(cm^2 s)$ and Fig. 5 for $M = 0.8\,\mu A/(cm^2 s)$. In both cases, we examine the situations with $E_K = -25\,mV$ and $-45\,mV$. We classify the spiking behavior of the soma using two characteristics: (1) whether or not a particular waveform (a single spike or

[2] $R^2 \equiv$ 1- (sum square of residuals)/ (sum square of differences of the dependent variable from the mean).

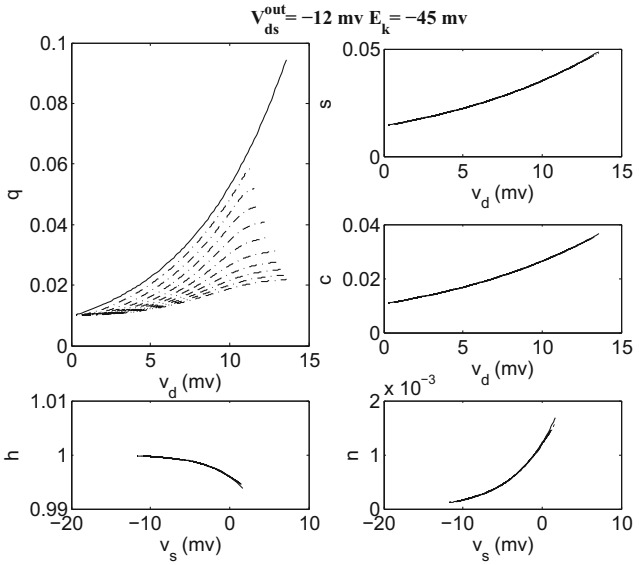

Fig. 13 The q gating variable is the only gating variable sensitive to M over the range considered here. The five gating variables of the polarized PR neuron are shown as the neuron is taken from rest to a somatic potential spike in response to a range of injected ramp currents. In each case $V_{ds}^{out} = -12\,mV$ and $E_k = -45\,mV$. For each plot, the equilibrium value is denoted by a solid line, and the computational results are denoted by dashed lines. There are ten different dashed lines corresponding to M from $0.1\ \mu A/(cm^2 s)$ to $1.0\ \mu A/(cm^2 s)$. Only the slowly-activating q gating variable exhibits significant deviation from the equilibrium curve. In all other plots, the gating variables track the equilibrium curve so closely, regardless of the injection rate, that the lines can barely be distinguished. Note that although q is a function of Ca the fact that Ca equilibrates with changing V_d well over an order of magnitude faster than q equilibrates with changes in Ca allows us to approximate the q kinetics $q(Ca(V_d))$ by $q(Ca_\infty(V_d))$

burst of activity) repeats periodically over a long duration ($> 20ms$) or if it is limited to a single spike or burst of activity, and (2) by the number of individual spikes occurring within a particular waveform. For periodicity, we classify the activity as a single burst or spike if there is only one occurrence of a particular waveform within our run-time of 10 seconds and is denoted by an open symbol. The number of somatic membrane potential spikes in each waveform are encoded by the symbol shapes (see figure caption). A number of spiking behaviors are observed over the E_K and M values chosen. In particular, note that the sublinear profiles at weak polarizations exhibit periodic spikes or bursts, and at intermediate to strong polarizations, show only isolated spikes or bursts. In contrast, the superlinear profile exhibits isolated spikes at weak polarizations and becomes periodic towards the end of the intermediate polarization region. Thus, qualitative differences between sublinear and superlinear profiles appear in spiking behavior as well as the TTFS.

Figure 6 shows how the occurrence of sub- or superlinear TTFS profiles in the intermediate region depend more generally on E_k and M. The data points divide the parameter space into regions in which the system exhibits sub- and superlinear behavior in the intermediate polarization region where the second-derivative test is unambiguous (see Section 2.2.2). Note that the accuracy of the line dividing the sublinear and superlinear regions is limited by our choice of discretization in M (i.e., steps of size $0.05\ \mu A/(cm^2 s)$).

Note that for the sublinear case shown in Fig. 3b the TTFS curve turns over and begins to decrease with increasingly negative V_{ds}^{out}. A more complete view of this behavior is shown in Fig. 7, which shows the TTFS over a full range of stable polarizations for the fast injection rate ($M = 0.8\ \mu A/(cm^2 s)$). Even for the superlinear case the overall tendency is for the TTFS to decrease in the strong polarization region. For a superlinear profile the TTFS reaches several seconds or more in the strong polarization region. An interesting pattern emerges which includes sudden changes in TTFS (not shown). This complex profile occurs due to interactions of the very slow decay rate of the I_{K-AHP} and the ramp injection protocol. While interesting, these results might be difficult to replicate experimentally.

We define the polarization at which the TTFS begins to decrease with increasingly negative V_{ds}^{out} as the beginning of the strong polarization region. We then refer to the region between the weak and strong polarization as the intermediate region.

Figures 3, 6, and 7 show how the polarization-dependent excitability varies over a range of extracellular potassium and current injection rates. In summary, we catergorize polarization as follows:

1. Weak polarization – in this region, the TTFS increases linearly with increasingly negative polarization (*i.e.* increasing somatic hyperpolarization). This corresponds to a V_{ds}^{out} ranging from about $10\,mV$ to $-4\,mV$.
2. Intermediate polarization – In this region, the TTFS departs from its linear dependence on polarization. The TTFS increases either sublinearly or superlinearly with polarization, depending on the values of M and E_K.
3. Strong polarization – In this region, the TTFS decreases with increasingly negative polarization. The strong polarization region begins around a V_{ds}^{out} equal to about $-15\,mV$, but this onset depends on the chosen parameters.

We now take a closer look at the three regions, and most significantly, identify the mechanisms that give rise to the

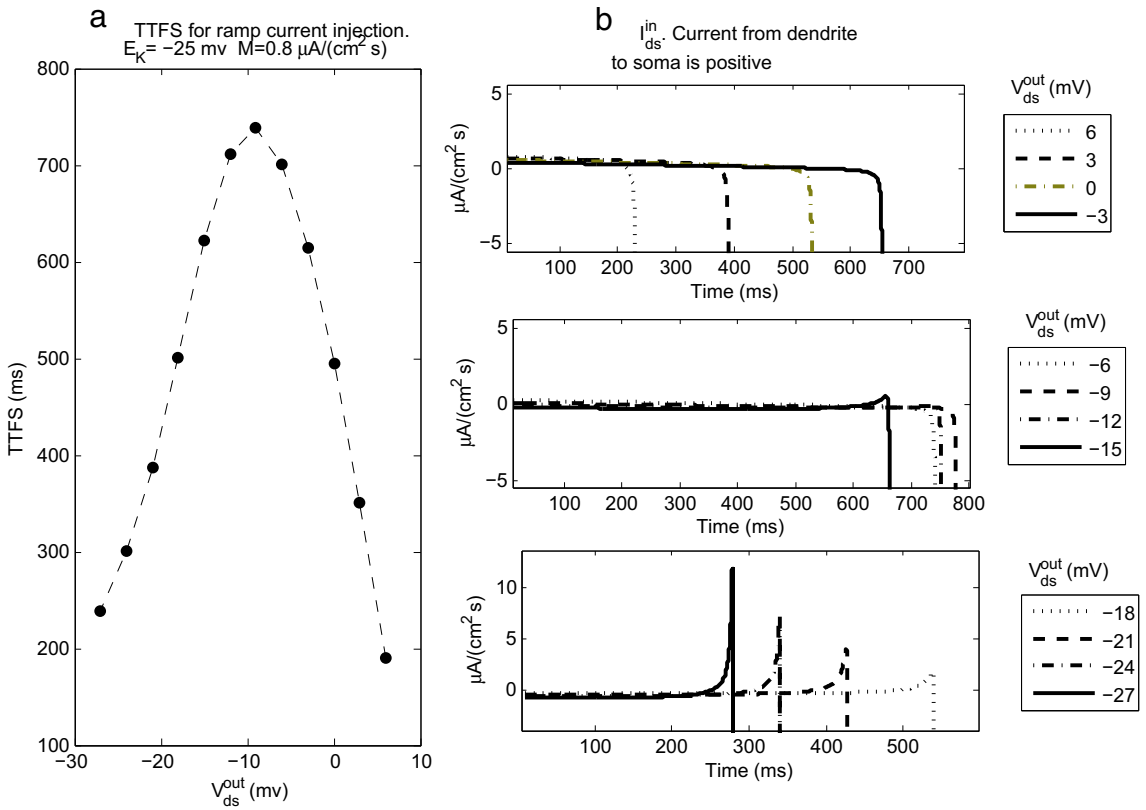

Fig. 14 In the strong polarization region, where TTFS decreases, a dendritic spike precedes the somatic potential spike. Somatic and dendritic potential spikes are revealed when plotting I_{ds}^{in}. Plots of the current flow between compartments, $g_c(V_d - V_s + V_{ds}^{out})$ are shown in (**b**) for the corresponding V_{ds}^{out} shown in (**a**). Spikes in V_d result in positive current spikes in (**b**) while spikes in V_s result in negative current spikes in (**b**). Since for each polarization the applied current ramp grows until the somatic potential spike in all cases the I_{ds}^{in} ends with a negative spike. The appearance of dendritic spikes (positive I_{ds}^{in}) coincides with the decreasing TTFS. Evidently the increase in depolarizing current coming from the dendrite back into the soma more than compensates for the increased soma-hyperpolarizing V_{ds}^{out}

observed TTFS behavior in the intermediate and strong regions.

3.2 Weak polarization region

The TTFS behavior of our polarized PR model is linear at weak polarizations and is in agreement with experimental observations (Bikson et al. 2004; Radman et al. 2007, 2009).

3.3 Intermediate polarization region

As V_{ds}^{out} becomes more negative, the resting potential of the dendrite becomes more depolarized. Starting from a more depolarized state, more of the dendritic channels are open, and the dendrite as a whole is primed for activity with the incoming soma current injection. We will show that the division of the solutions into either sublinear or superlinear profiles is due to the active currents in the dendrite. We note that I_{KAHP} and I_{KC} are functions of E_K, while I_{Ca} does not have any explicit dependence on E_K. In addition, M only affects the slow q-gating variable of I_{KAHP}. It is the modulation, through E_K and M, of the strength of the hyperpolarizing dendritic currents that is responsible for the occurrence of sub- or superlinear TTFS profiles. The following observations and deductions lead us to this conclusion:

(1) Except for the strong polarization case, the soma was always found to spike before the dendrite.
(2) Prior to an action potential, the somatic and dendritic membrane potentials rise at the same rate in response to the soma-injected current ramp for all parameters tested in our numerical simulations. This is to be expected due to the high inter-compartment conductance, g_c, and rapid equilibration compared to the

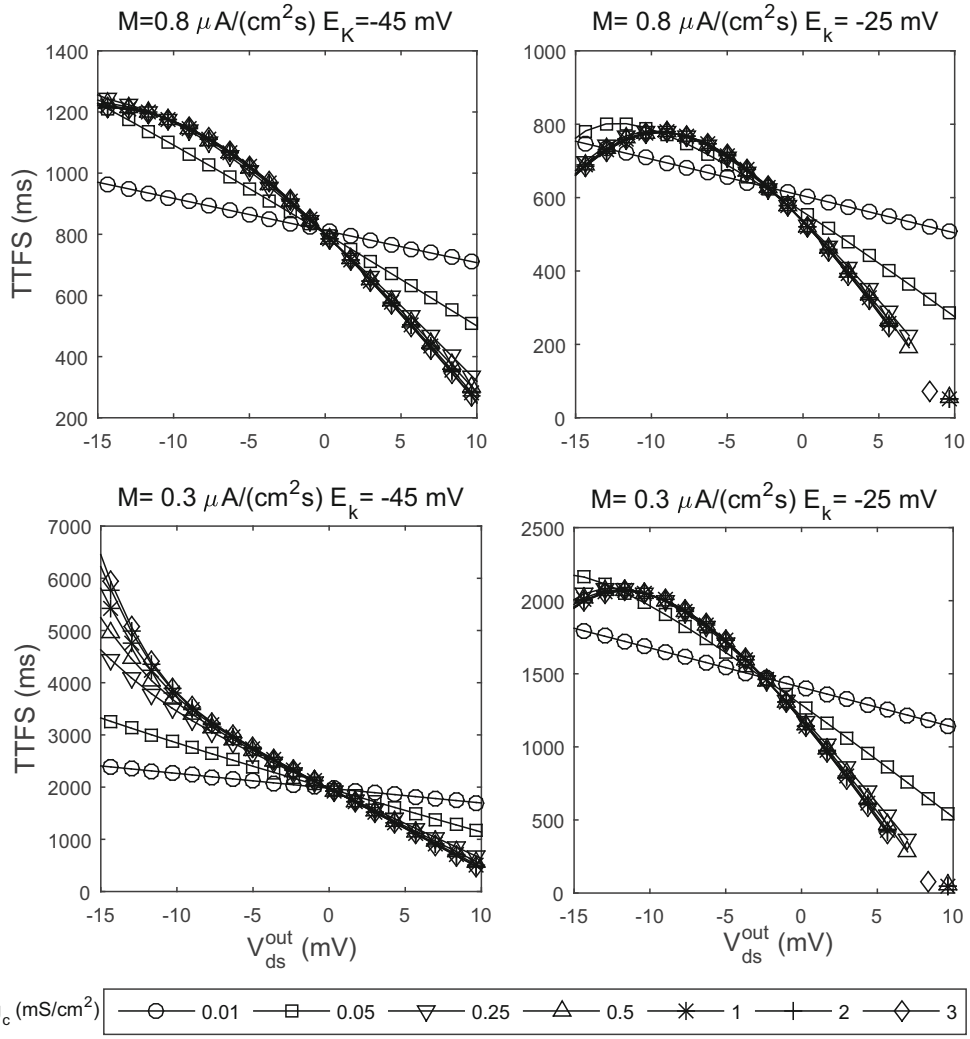

Fig. 15 TTFS profiles for various values of g_c, the electrotonic coupling between the soma and the dendrite

current injection rate. The membrane potentials continue to rise at the same rate until a spike occurs,[3] To show that indeed $dV_s/dt \approx dV_d/dt$, we examined the right-hand side of dV_s/dt and dV_d/dt for various values of E_K, M, and V_{ds}^{out}. We found that the total somatic and dendritic currents are indistinguishable for even the fastest ramp we explored, $M = 0.9\mu A/(cm^2 s)$ (see Fig. 8).

(3) Significantly more current is shunted away from the soma and into the dendrite for the superlinear case compared to the sublinear case. This is shown in Fig. 9. It might be inferred that the increase in the shunting current in the superlinear cases is due to an increase in hyperpolarizing outward dendritic current. Support for this assertion can be found by plotting the total active dendritic current for the sublinear and superlinear cases, respectively. Figure 10 shows how differently the active dendritic currents of a sublinear and superlinear profile vary with time and over a range of intermediate polarizations. For the sublinear cases, the active dendritic currents monotonically increase and result in a net depolarizing effect over the range of intermediate polarization. However, for the superlinear case, the active dendritic currents depolarize very slowly from $-10mV$ to $-12mV$ and become non-monotonic, eventually resulting in a net hyperpolarizing effect at negative polarization values below -13 mv.

[3]The rate of change of the somatic and dendritic membrane potentials are appreciably different only in a 1-2 millisecond period after the TTFS and during an action potential.

(4) The effect that polarization has on the rate at which the soma depolarizes can be analyzed by examining the active and total dendritic currents (since $dV_s/dt \approx dV_d/dt$). At intermediate polarization (Fig. 11) we see that the total dendritic current is significantly reduced for the superlinear case and delays the TTFS as compared to the sublinear case. In contrast, at weak polarization, when the voltage-activated gating variables are minimal and have yet to begin their rapid ascent we see in Fig. 12 that the sublinear and superlinear cases do not exhibit such qualitative differences in their dendrititic currents.

(5) Finally, we note that the division of the $E_K - M$ parameter space into sublinear and superlinear profiles corresponds to a separation into stronger and weaker dendritic hyperpolarizing currents. The effect of lowering the potassium reversal potential E_K can be understood by examining the equations for the polarized PR neuron Eqs. (3–5) and noting that for all potassium currents in both the dendrite and the soma, a more negative E_K corresponds to a stronger drive for positive current to flow out of the compartments. The role of M is made clear by examination of the gating kinetics. We plotted the gating variables during our ramp-stimulation protocol over a range of M and we see that M only affects the very slow q-gating variable of the I_{K-AHP} current (Fig. 13). With a lower M, the slow equilibrating q-gating variable has more time to reach its equilibrium value. Since q is monotonically increasing with V_d, and V_d is always increasing during the ramp somatic current injection (at least for the range of parameters we examined), q will always be in the process of equilibration to a higher value. Thus the lower M is, the greater q gets, and the greater the hyperpolarizing I_{K-AHP} current will become.

In summary: As polarization becomes increasingly negative, the dendritic calcium currents increasingly depolarize the dendrite. Simultaneously, the dendritic potassium currents increasingly hyperpolarize it. Thus, these currents

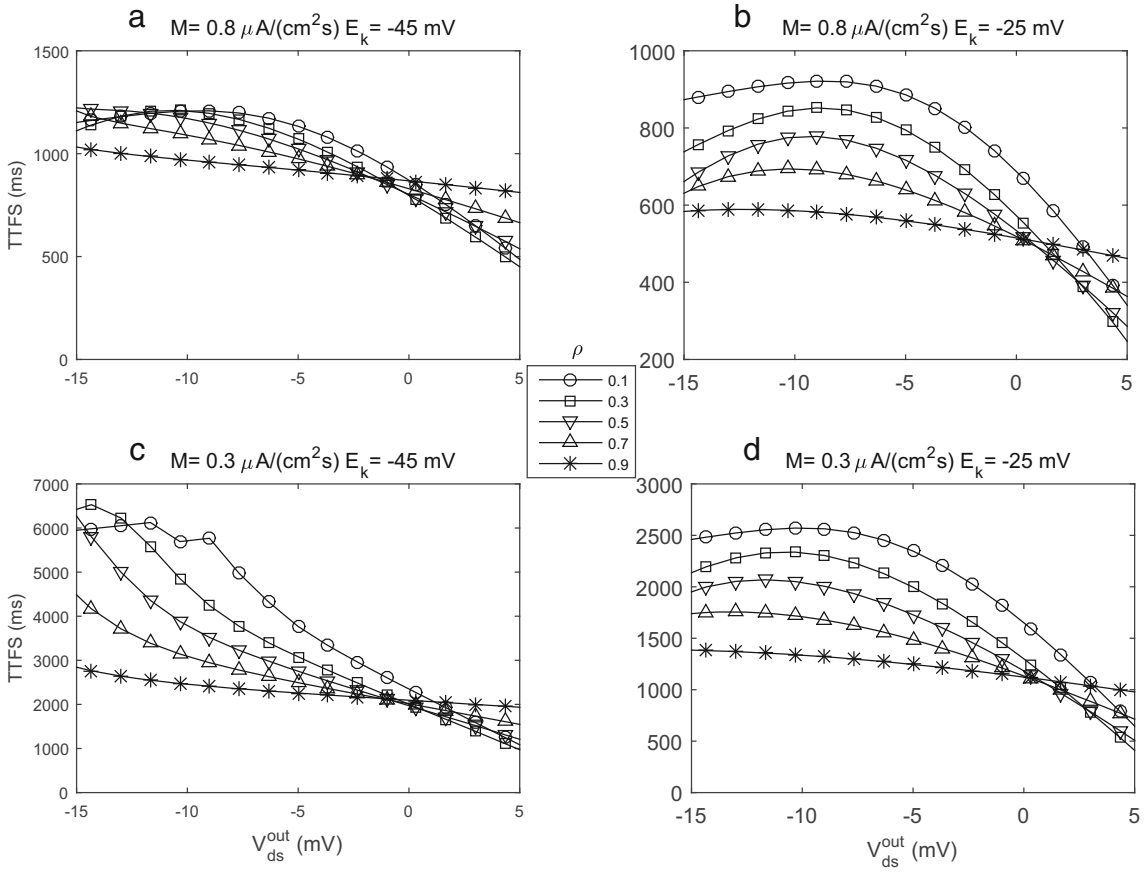

Fig. 16 The proportion of the total membrane area allocated to the soma compartment, ρ, is varied over a range from 0.1 to 0.9

have competing effects: one works to excite, the other to inhibit. If the calcium current dominates, then we observe a sublinear response, and if the potassium current dominates, we observe a superlinear response.

3.4 Strong polarization region

The mechanism behind the decrease in the TTFS (as V_{ds}^{out} decreases) at strong polarizations is revealed by examining the shunting current from the soma to the dendrite. Figure 14 plots this shunting current, I_{ds}^{in}, with negative values indicating positive charge flowing from the soma to the dendrite and positive values indicating the reverse. Since in all cases the stimulus ends when the soma spikes, all the curves end with a sharp negative drop. However, corresponding to the strong polarization values at which the TTFS begins to decrease, positive deflections in I_{ds}^{in} are seen in increasing magnitude (see the two right lower panels in Fig. 14). These positive deflections result from dendritic spikes back-propagating into the soma. These then act as a depolarizing trigger which induces a soma spike. I_{Ca} is the only active depolarizing dendritic current, and it is this current that is responsible for the dendritic potential spikes and subsequent decrease in the TTFS.

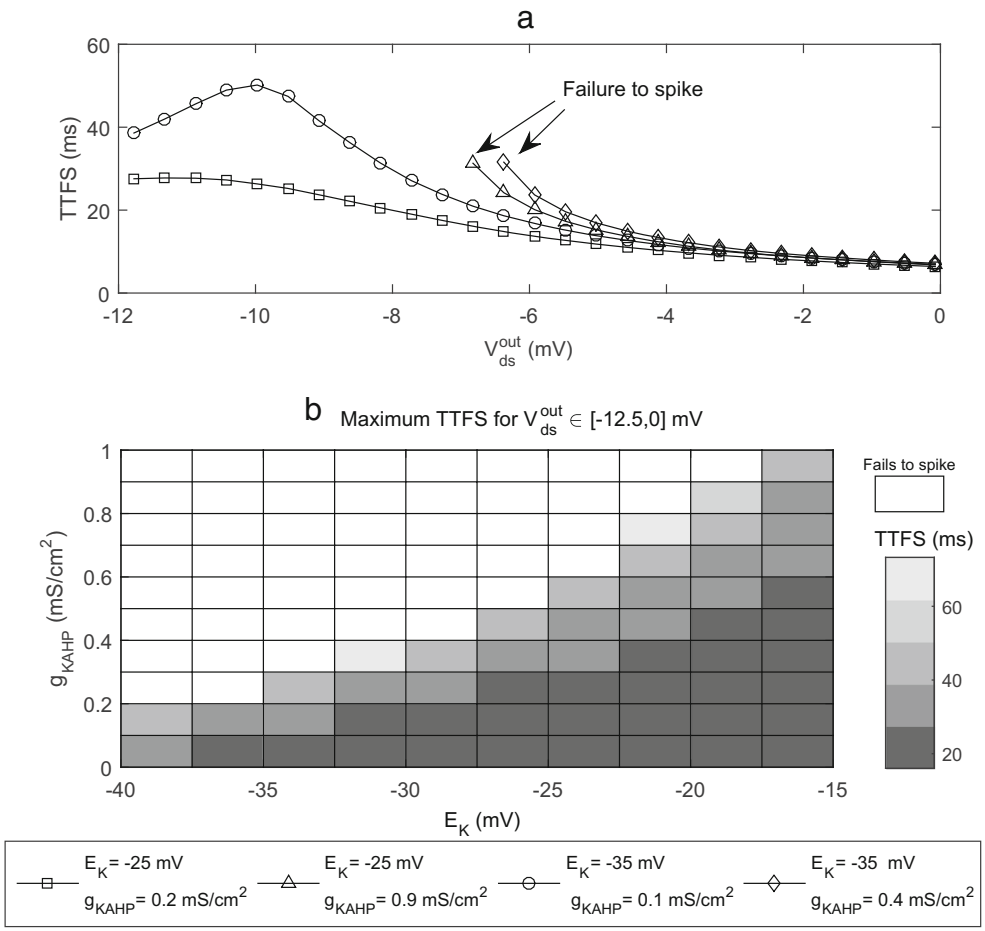

Fig. 17 For our synaptic AMPA protocol ($g_{AMPA} = 0.3mS/cm^2$) we find a clear split in the $g_{KAHP} - E_K$ parameter space into neurons that fail to spike at some point in the intermediate range and those that have a spiking solution into the strong polarization region. In (**a**) we have plotted the maximum TTFS obtained in the intermediate polarization region, which we defined as $V_{ds}^{out} \in [-12.5, 0]$ mV since this encompassed all of the polarization values capable of producing a maximum TTFS. Polarization values were stepped by 0.075 mV. In (**b**) we plot the TTFS profiles for four sets of $E_K - g_{KAHP}$ values. Two of them are in the "Fail to spike" region in (a) (white) and two are in the shaded region indicating that they spike throughout the intermediate region and into the strong region. The line marked with circles ($E_K = -35$ mV and $g_{KAHP} = 0.1ms/cm^2$) is close to the boundary and reaches a maximum at around -10 mV at which point by our definition it reaches the end of the intermediate region and the beginning of the strong region

3.5 Effects of morphology on excitability

We have used only one value for g_c ($2.1\ mS/cm^2$) and one for ρ (0.5) in our simulations so far. These values were used as standard values in Pinsky and Rinzel (1994). Biological pyramidal neurons are most likely not so electro-tonically "close", and the dendritic and somatic areas may vary substantially. To gauge the sensitivity of our results to variation of these morphological parameters, we systematically varied g_c and ρ for the ramp injection protocol. Results are shown in Figs. 15 and 16 respectively. To understand how g_c effects the TTFS in Fig. 15 it helps to think of the path of the injected soma current: (1) out of the soma through the membrane (i.e., leak) (2) into the dendrite, and (3) from the dendrite out through the dendritic membrane. We can neglect (1) since the leak current is small compared to the inter-compartment conductance and the membrane currents. For very small g_c (see circles and squares in Fig. 15a–d the linearity of the TTFS as a function of V_{ds}^{out} can be explained by the inter-compartment current, $I_{ds} = g_c(V_d - V_s + V_{ds}^{out})$, becoming dominant. For moderate and higher levels of g_c, the current leaving through the dendrite via the nonlinear active dendritic membrane currents play an increasing role as we go through the intermediate and strong polarization regions. In this case, the calcium and hyperpolarizing potassium currents become increasingly active, and the TTFS profiles display the same qualitative shapes we saw earlier for $g_c = 2.1 mS/cm^2$ (Fig. 3).

Figure 16 shows how varying the proportion of total membrane area allocated to the soma, ρ, affects the TTFS as a function of V_{ds}^{out}. The qualitative features of the TTFS profiles are consistent with the profile for $\rho = 0.5$. Because

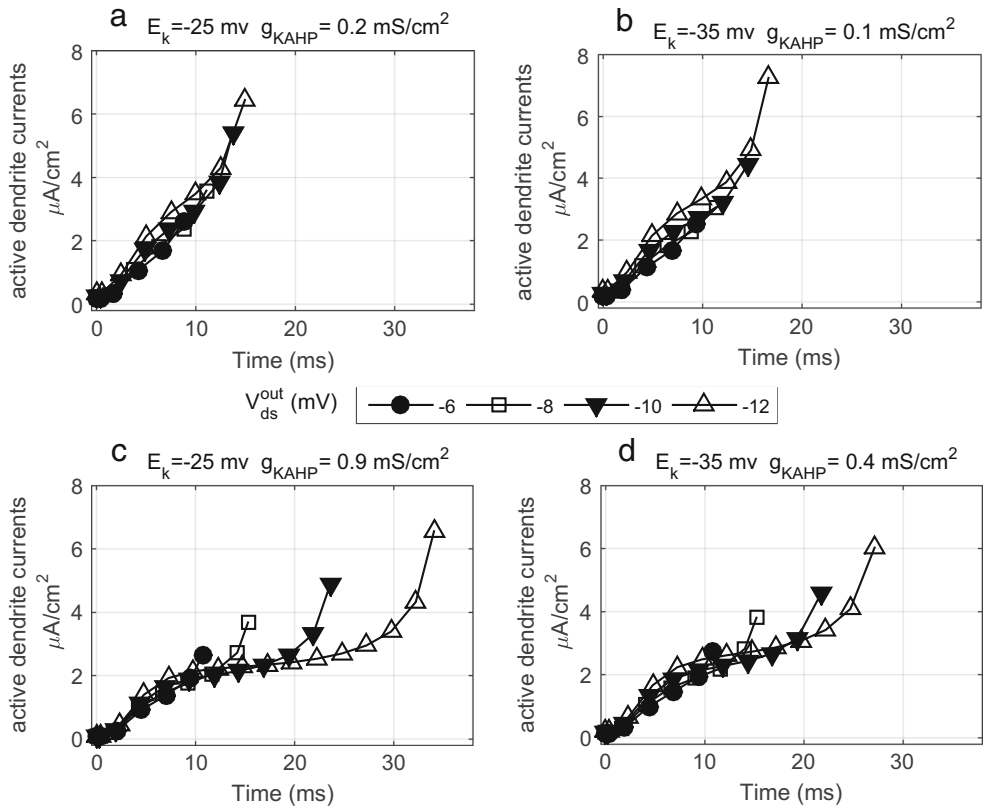

Fig. 18 For the AMPA current protocol, the neurons that fail to spike in the intermediate region and those that do is correlated with a qualitative change in the total active dendritic current. The sets of $E_K - g_{KAHP}$ values in (**a**)–(**d**) are the same as in Fig. 17b. For the two neurons that spike throughout the intermediate region, (**a**) and (**b**), The total active dendritic current grows linearly and at nearly the same rate regardless of the polarization. In contrast, for the two neurons that failed to spike the total active dendritic current, after about 10 ms, grows at a much slower rate and shows more pronounced polarization dependence. These observations are consistent with our observations and hypothesis made using the ramp injected protocol about the role of the active dendrite currents. One difference between the ramp injected protocol and the AMPA protocol is that for the ramp injected protocol the total active dendritic current become net hyperpolarizing in the superlinear case (Figs. 10 and 12)

of the mismatch in load at $\rho = 0.9$ (stars in (a-d)), more of the current remains in the soma, and it is the linear dependence of I_{ds} on V_{ds}^{out} that contributes to a more linear TTFS profile. As $\rho \rightarrow 0$, the current flows increasingly into the dendrite where the nonlinear dendritic membrane currents affect the TTFS.

3.6 Polarization-dependent excitability using synaptic AMPA

The preceding results were based on the use of an injected ramp current, delivered at various rates, primarily to facilitate comparison with experiments. The ramp injected current is a commonly-used protocol for characterizing neural excitability. However, it is also of interest to examine how polarized neurons respond to synaptic inputs.

Accordingly, we replaced the ramp current injection with synaptic AMPA currents in the dendritic compartment using the same synaptic model for AMPA as in Pinsky and Rinzel (1994) and Park et al. (2003, 2005). In the intermediate region, the shape of somatic spikes change somewhat with increasing polarization, as was shown in Figs. 4 and 5. Thus, we would expect polarization-dependent effects on the synaptic current based on the model described above. However, to facilitate the following analysis, we fix the presynaptic activity to consist of a single spike such that $V_{s,pre}$ is above 20 mV for 1.2 ms.

The main difference between this approach and the ramp current protocol is that in the synaptic input case, a failure to spike is an important possible outcome. This is illustrated in Fig. 17, using $g_{AMPA} = 0.3mS/cm^2$ and $I_{s,inj} = 0.5\mu A/cm^2$. Panel (a) shows the TTFS versus V_{ds}^{out} profiles for two cases (with parameters E_K and g_{KAHP}) in which the curve terminates because the neuron fails to spike. The same panel shows two other cases in which the TTFS profile could be obtained throughout the range of V_{ds}^{out} studied.

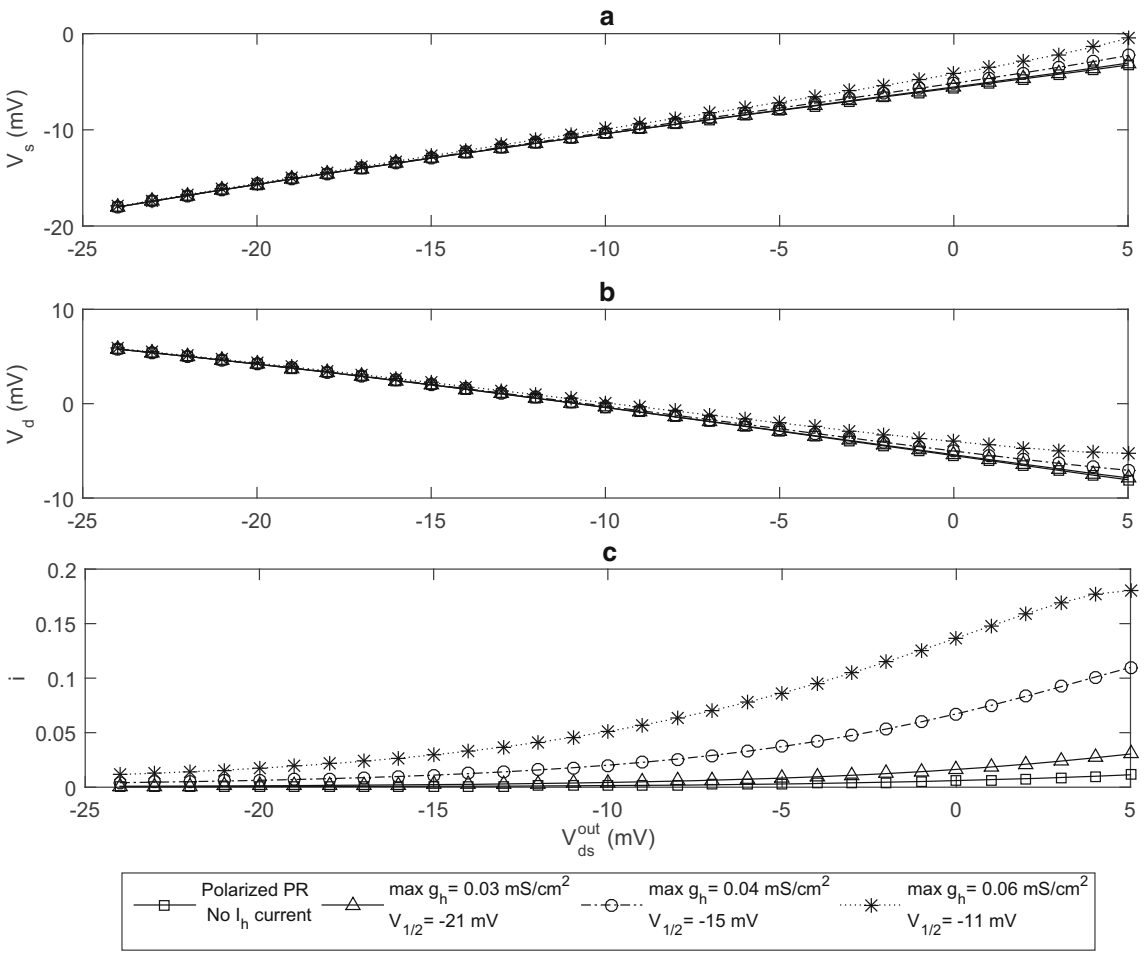

Fig. 19 This figure shows V_{ds}^{out} versus V_s, V_d, and i for the resting state (**a**)-(**c**) respectively

Panel (b) shows the maximum TTFS obtained over $V_{ds}^{out} \in [-12, 0]$ mV, as a function of g_{KAHP} and E_K, noting the cases in which the neuron fails to spike somewhere in the V_{ds}^{out} range. Polarization values were stepped by 0.075 mV. We find a clear division of this parameter space into a region corresponding to spike failure, and a region for which spikes occur throughout the V_{ds}^{out} range and a value of the maximum TTFS can be obtained. The values of g_{KAHP} at the boundary increase with increasing E_K, as the increased excitability due to extracellular potassium is somewhat balanced by an increase in hyperpolarizing K_{AHP} conductance.

In Fig. 18, we see that the segregation of cases that fail to spike and those that do spike is correlated with a qualitative change in the total active dendritic currents. The sets of E_K and g_{KAHP} values in (a)–(d) are the same as in Fig. 17a. For the two cases without spike failure (panels (a) and (b)), the total active dendritic current grows linearly and at nearly the same rate roughly independently of the polarization. In contrast, for the two cases with spike failure (panels (c) and (d)), the total active dendritic current after about 10 ms grows at a much slower rate and shows more pronounced polarization dependence. These observations are consistent with our previous observations using the ramp current protocol regarding the role of the active dendritic currents. In particular, neurons that were superlinear for the ramp protocol and those that failed to spike for the AMPA protocol were associated with similar total active dendritic currents. Namely, the total active dendritic currents are significantly suppressed, polarization-dependent, and were modulated by the potassium-dependent hyperpolarization currents.

3.7 Inclusion of I_h current

The concentration of I_h channels is many times higher in the dendritic portion of pyramidal cells than in the somatic

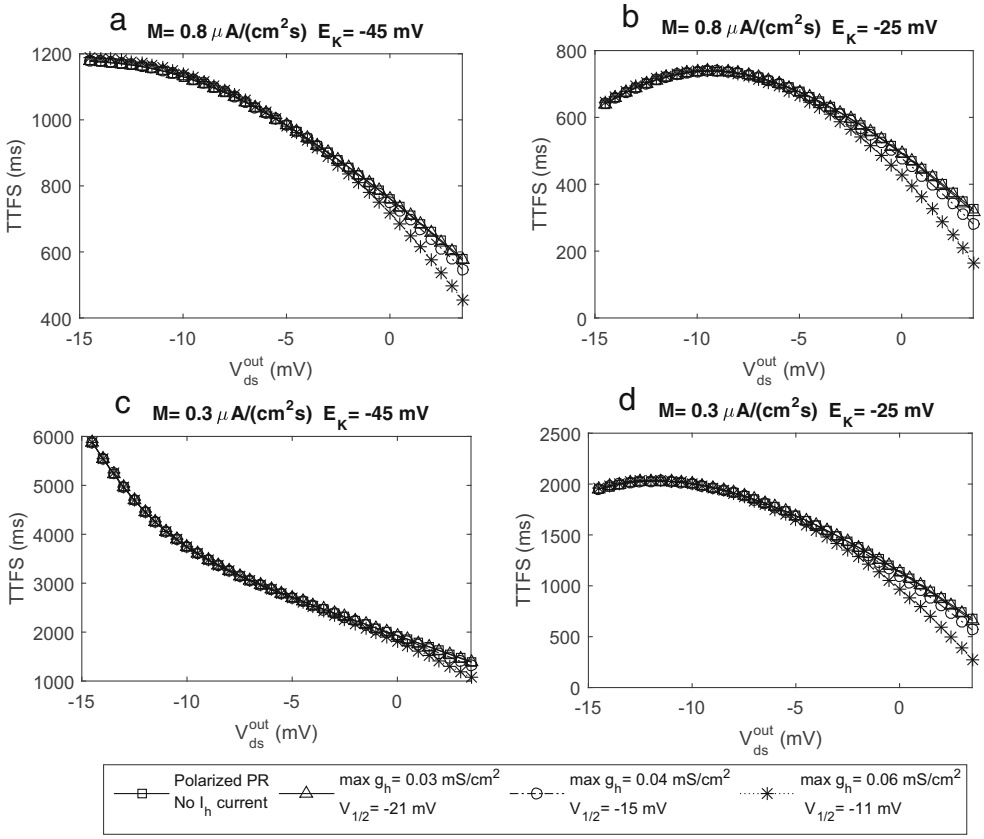

Fig. 20 The ramp injected protocol with polarized PR model plus I_h current. The differences between the polarized PR without I_h (*square*) and the different regulated states of I_h (*triangle*, *circle*, *star*) are most apparent at larger V_{ds}^{out} and at more hyperpolarized dendritic membrane potentials. Also apparent is the significant gap between what has been treated as the high up-regulated state from serotonergic studies (Gasparini and DiFrancesco 1999) (*circle*) and the most active state used in Lippert and Booth (2009) (*star*)

region (Dyhrfjeld-Johnsen et al. 2009). We therefore equip our existing polarized PR model with an I_h current in the dendritic compartment. The I_h current is activated at hyperpolarizing potentials, is active at rest, has moderately long time constants, and can obtain various regulated states. These regulated states are simulated by adopting various values of the maximal conductance g_h and the channel half-activation voltage V_{i-half}. The equations and parameters are given in the Methods section.

In the following computations, except for the inclusion of the I_h current, all other parameters and currents remain the same as in previous ramp-injected and AMPA-injected computations. First, we show how the resting membrane potentials change with the inclusion of I_h at different levels of regulation. Figure 19 depicts the somatic and dendritic potential and the I_h gating variable i ((a)-(c) respectively) as a function of V_{ds}^{out}. The changes in resting membrane potential coincide with the activation of i at hyperpolarized values of V_d occurring at more positive V_{ds}^{out}. The effect is greater at more up-regulated states when g_h and V_{i-half} are increased. We next examine how the various regulated states of the I_h current affect our ramp-injected protocol results. In Fig. 20 we performed computations analogous to those of Fig. 3 depicting the polarization-dependent TTFS for high and low E_K and for fast and slow M. The results are qualitatively similar to those in Fig. 3, which had no I_h currents. The small differences between the polarized PR without I_h (square) and with I_h (circle, triangle, star) are most apparent for larger V_{ds}^{out}, corresponding to more hyperpolarized dendritic membrane potentials. Also apparent is the significant gap between what has been treated as the high-level up-regulated state from serotonergic studies (Gasparini and DiFrancesco 1999) (circle) and the most active state used in Lippert and Booth (2009) (star).

In Fig. 21, the AMPA protocol is used as in Fig. 17. We compare the polarized PR neuron without I_h (a) to the polarized PR neuron with I_h at two up-regulated levels (b) and (c). The clear split in the g_{KAHP}-E_K plane into those neurons that have a spiking solution throughout the intermediate region and those that fail at some intermediate polarization is present both without I_h (a) and with I_h currents at both the control state (b) and the extreme activation range used in Lippert and Booth (2009) (c). In (b) and (c) the depolarizing effect of I_h is apparent in the diminishing area of spike failure and the decreasing TTFS.

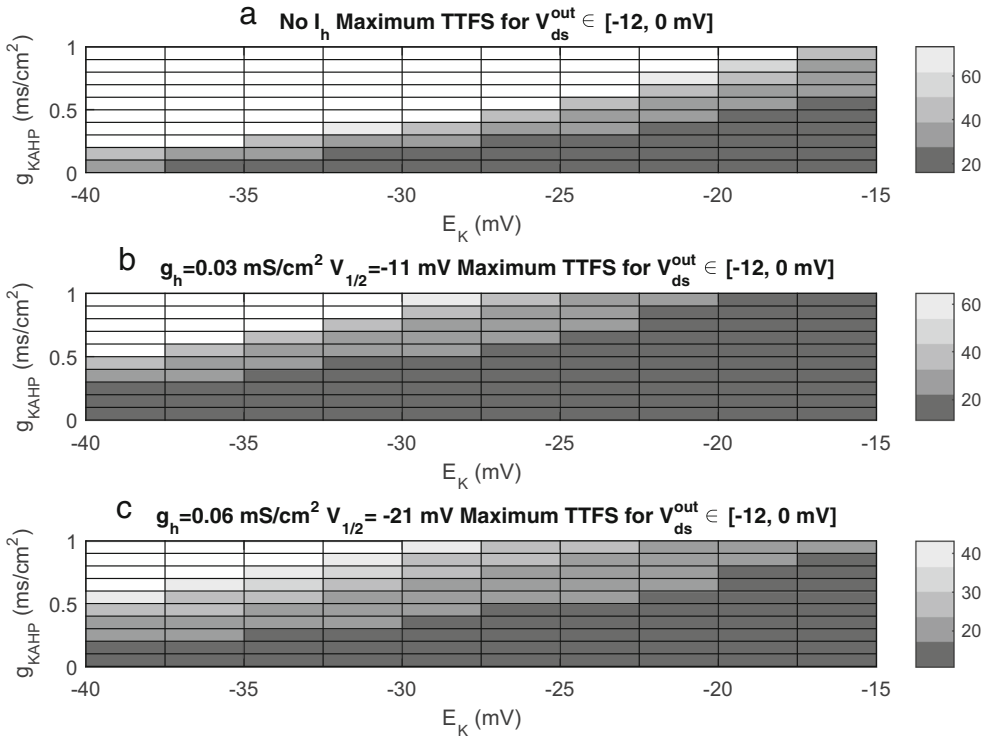

Fig. 21 TTFS for different levels of I_h, where darker is faster spiking and white denotes spike failure. The spike failure profile persists with added I_h, but the depolarizing effect of I_h causes quicker TTFS and decreases the size of the spike failure region

4 Discussion

There is experimental evidence of a weak polarization region where the excitability decreases linearly with increasing soma-hyperpolarizing polarization (Bikson et al. 2004; Radman et al. 2007, 2009). In addition, a strong polarization region has been found where the excitability increases with stronger soma-hyperpolarizing polarization (Bikson et al. 2004). We are unaware of any theoretical or experimental work exploring excitability at intermediate polarizations. Our results provide experimentally-testable predictions of how neuronal excitability is affected by polarization. The boundaries of the polarization regions and the $E_K - M$ bifurcation values will undoubtedly vary from neuron to neuron, reflecting variations in their density of channels and even changes in their activation potentials. However, the qualitative structure of polarization-dependent excitability that we have shown might well serve as an initial working hypothesis.

Several consequences follow from our results. First, once outside the weak polarization region, efforts to control the dynamics of a neuron or a network of neurons may depend critically on whether the neuron(s) has (have) a sublinear or superlinear TTFS sensitivity to polarization. In particular, the ability of $[K^+]_o$ to drive the neuron to and from a sublinear and superlinear dependence on polarization might suggest that the extracellular potassium and its dynamics may need to be considered when trying to modulate neural activity with electric fields. As we have mentioned, neural hyperactivity has been shown to lead to an increase in $[K^+]_o$, thus increasing E_K (Janigro 2006; Binder et al. 2006; Dietzel et al. 1989) which in turn further increases neural excitability. The neural activity and extracellular potassium levels by themselves form a positive feedback loop. However, application of increasingly soma-hyperpolarizing fields will, in the weak and intermediate regions, decrease excitability. The decreased excitability would be expected to decrease $[K^+]_o$ and hence decrease the polarization-dependent excitability induced by soma-hyperpolarizing fields, thus resulting in a negative feedback loop. Further still, if the decrease in $[K^+]_o$ is sufficient to draw neurons from a sublinear to superlinear profile, then we might expect to see a sudden step-down in excitability and a qualitative change in the rate at which excitability is decreased with polarization strength.

Second, outside the weak polarization region we found that channels and their currents, which are normally associated with a neuron in its active spiking or bursting state, can also significantly influence its subthreshold excitability. Third, we found that although the values of q (gating variable for the dendritic K_{AHP} current) obtained during subthreshold stimulus are small (being no more than about 0.05 of the maximum, compared to near 1 during the burst), results in Fig. 6 indicate that the variation in q with M is significant enough to effect a transition between sublinear and superlinear TTFS profiles.

The observation that a small fraction of activated channels can have significant influence on the excitability of a polarized neuron places a particular importance on the nascent stages of channel activation. For computational ease many models truncate the early stages of channel activation (or simply replace more complex functions with sigmoidal or step functions). These modifications may have little effect on spike trains of unpolarized or weakly polarized neurons, however, they will most likely fail to accurately depict polarization-dependent excitability outside of the weak polarization regime.

The ramp injection rate M may model actual applied ramp currents, or it may approximate the convolution of many pre-synaptic inputs to the dendrite. Results differ only slightly when the somatic injection is replaced by dendritic injection in the model and is less significant when g_c is larger (data not shown). For the ramp injected current protocol, we have shown that slower sustained input allows for more time for the very slow K_{AHP} gates to open, thus facilitating hyperpolarization and potential superlinear profiles. These superlinear profiles may also be obtained by varying either or E_K and g_{KAHP}. In addition, we showed further evidence that the dendritic spikes at strong polarization cause a reversal in excitation (i.e., decreasing TTFS with decreasing V_{ds}^{out}) and we note that this is due to the same calcium currents that are responsible for the back-propagation that sustains a burst (Bose and Booth 2004). In summary, our results suggest that the activation or partial activation of dendritic currents critical to pyramidal cell burst dynamics also play an important role in shaping the polarization-dependent excitability of a neuron.

We chose a two-compartment model to facilitate our analysis. It would be interesting to see how a more complex multi-compartment model would behave. For example, a model with apical and basilar dendritic compartment on either end of a soma compartment would allow for the possibility of injected current taking two paths out of the soma. Although the degree of polarization from the soma to the apical dendrites may be significantly reduced. A possible extension of this study would include a multi-compartment model such as Traub et al. (1991)'s 19-compartment CA3 pyramidal model with a graded distribution of currents and possibly additional types of currents.

Finally, looking at our results abstractly beyond the framework of a particular neuron or model neuron, we speculate on the question of what it takes for a neuron to exhibit the characteristics of the weak, intermediate, and strong polarization regions observed in our study using the polarized PR-model. We conjecture that (1) without

a depolarizing dendritic current any reversal in excitability seen at strong polarization would be impossible, (2) the ranges of the weak, strong and intermediate regions depend on how the channels activate with membrane potential, and (3) that the clear division in the polarization-dependent excitability seen in the intermediate region requires two competing currents, one depolarizing and one hyperpolarizing.

Acknowledgments We wish to thank the reviewers for their careful review and insightful suggestions.

Conflict of interests The authors declare that they have no conflict of interest.

References

Barreto, E., & Cressman, J. (2011). Ion concentration dynamics as a mechanism for neuronal bursting. *Journal of Biological Physics*, *37*(3), 361–373. doi:10.1007/s10867-010-9212-6.

Berzhanskaya, J., Gorchetchnikov, A., & Schiff, S.J. (2007). Switching between gamma and theta: Dynamic network control using subthreshold electric fields. *Neurocomputing*, *70*(10-12), 2091–2095. doi:10.1016/j.neucom.2006.10.124, http://www.sciencedirect.com/science/article/B6V10-4M9Y1V1-G/2/05a532a351f790864e8ff5511052b9c3, computational,neural circuitry.

Bikson, M., & Rahman, A. (2013). Origins of specificity during tDCS: anatomical, activity-selective, and input-bias mechanisms. *Frontiers in Human Neuroscience*, *7*, 688. doi:10.3389/fnhum.2013.00688.

Bikson, M., Inoue, M., Akiyama, H., DJ, K., Fox, J., Miyakawa, H., & Jefferys, J. (2004). Effects of uniform extracellular dc electric fields on excitability in rat hippocampal slices *in vitro*. *Journal of Physiology*, *557*(1), 175–190.

Binder, D., Yao, X., Zador, Z., Sick, T., Verkman, A., & Manley, G. (2006). Increased seizure duration and slowed potassium kinetics in mice lacking aquaporin-4 water channels. *GLIA*, *53*(6), 631–636. doi:10.1002/glia.20315.

Bose, A., & Booth, V. (2004). Bursting in 2-compartment neurons: A case study of the Pinsky-Rinzel model. Center for Applied Mathematics and Statistics.

Cressman, J., John, R., Ullah, G., Ziburkus, J., Schiff, S., & Barreto, E. (2009). The influence of sodium and potassium dynamics on excitability, seizures, and the stability of persistent states: I. single neuron dynamics. *Journal of Computational Neuroscience*, *26*(2), 159–170. doi:10.1007/s10827-008-0132-4.

Cressman, J., Ullah, G., Ziburkus, J., Schiff, S., & Barreto, E. (2011). Erratum to: The influence of sodium and potassium dynamics on excitability, seizures, and the stability of persistent states: I. single neuron dynamics. *Journal of Computational Neuroscience*, *30*(3), 781–781. doi:10.1007/s10827-011-0333-0.

Csicsvari, J., Jamieson, B., Wise, K., & Buzsaki, G. (2003). Mechanisms of gamma oscillations in the hippocampus of the behaving rat. *Neuron*, *37*(2), 311–322. doi:10.1016/S0896-6273(02)01169-8.

Deans, J.K., Powell, A.D., & Jefferys, J.G.R. (2007). Sensitivity of coherent oscillations in rat hippocampus to ac electric fields. *Journal Of Physiology-London*, *583*(2), 555–565. doi:10.1113/jphysiol.2007.137711.

Dietzel, I., Heinemann, U., & Lux, H. (1989). Relations between slow extracellular potential changes, glial potassium buffering, and electrolyte and cellular-volume changes during neuronal hyperactivity in cat brain. *Glia*, *2*(1), 25–44. doi:10.1002/glia.440020104.

Dyhrfjeld-Johnsen, J., Morgan, R.J., & Soltesz, I. (2009). Double trouble? Potential for hyperexcitability following both channelopathic up- and downregulation of i(h) in epilepsy. Frontiers in neuroscience.

Francis, J.T., Gluckman, B.J., & Schiff, S.J. (2003). Sensitivity of neurons to weak electric fields. *The Journal of Neuroscience*, *23*(19), 7255–7261. http://www.jneurosci.org/cgi/reprint/23/19/7255.pdf.

Gasparini, S., & DiFrancesco, D. (1999). Action of serotonin on the hyperpolarization-activated cation current (I-h) in rat CA1 hippocampal neurons. European Journal of Neuroscience.

Ghai, R., Bikson, M., & Durand, D. (2000). Effects of applied electric fields on low-calcium epileptiform activity in the ca1 region of rat hippocampal slices. *Journal Of Neurophysiology*, *84*(1), 274–280.

Gluckman, B.J., Neel, E.J., Netoff, T.I., Ditto, W.L., Spano, M.L., & Schiff, S.J. (1996). Electric field suppression of epileptiform activity in hippocampal slices. *Journal of Neurophysiology*, *76*(6), 4202–4205. http://jn.physiology.org/cgi/content/abstract/76/6/4202, http://jn.physiology.org/cgi/reprint/76/6/4202.pdf.

Gluckman, B.J., So, P., Netoff, T.I., Spano, M.L., & Schiff, S.J. (1998). Stochastic resonance in mammalian neuronal networks. *Chaos: An Interdisciplinary Journal of Nonlinear Science*, *8*(3), 588–598. doi:10.1063/1.166340, http://link.aip.org/link/?CHA/8/588/1.

Gluckman, B.J., Nguyen, H., Weinstein, S.L., & Schiff, S.J. (2001). Adaptive electric field control of epileptic seizures. *Journal of Neuroscience*, *21*(2), 590–600. http://www.jneurosci.org/cgi/reprint/21/2/590.pdf.

Golding, T.K.Y.K.W.S.N., & Mickus, N.L. (2005). Factors mediating powerful voltage attenuation along ca1 pyramidal neuron dendrites. Journal of Physiology-London.

Han, C.L., Hu, W., Stead, M., Zhang, T., Zhang, J.G., Worrell, G.A., & Meng, F.G. (2014). Electrical stimulation of hippocampus for the treatment of refractory temporal lobe epilepsy. *Brain Research Bulletin*, *109*(0), 13–21. doi:10.1016/j.brainresbull.2014.08.007, http://www.sciencedirect.com/science/article/pii/S0361923014001336.

Holt, G.R., & Koch, C. (1999). Electrical interactions via the extracellular potential near cell bodies. *Journal of Computational Neuroscience*, *6*(2), 169–184. http://www.springerlink.com.mutex.gmu.edu/content/u262m146864wu008/fulltext.pdf.

Janigro, D. (2006). Brain water and ion fluxes: a hard-to-die hypothesis to explain seizure. Epilepsy Currents.

Lippert, A., & Booth, V. (2009). *Understanding effects on excitability of simulated I (h) modulation in simple neuronal models.* Biological Cybernetics.

McNamara, J. (1994). Cellular and molecular basis of epilepsy. *The Journal of Neuroscience*, *14*(6), 3413–3425. http://www.jneurosci.org, http://www.jneurosci.org/cgi/reprint/14/6/3413.pdf.

Mikkelsen, R., Andreasen, M., & Nedergaard, S. (2013). Suppression of epileptiform activity by a single short-duration electric field in rat hippocampus *in vitro*. *Journal of Neurophysiology*, *109*(11), 2720–2731. doi:10.1152/jn.00887.2012.

Miranda, P.C., Lomarev, M., & Hallett, M. (2006). Modeling the current distribution during transcranial direct current stimulation. *Clinical Neurophysiology*, *117*(7), 1623–1629. doi:10.1016/j.clinph.2006.04.009, http://www.sciencedirect.com/science/article/pii/S1388245706001726.

Moody, W.J., Futamachi, K.J., & Prince, D.A. (1974). Extracellular potassium activity during epileptogenesis. *Experimental Neurology*, *42*(2), 248–263. doi:10.1016/0014-4886 74)90023-5, http://www.sciencedirect.com/science/article/B6WFG-4BJW0K8-S5/2/5a1576e44b031b336a2de8069c9f4a03.

Park, E.H., So, P., Barreto, E., Gluckman, B., & Schiff, S. (2003). Electric field modulation of synchronization in neuronal networks. *Neurocomputing*, *52–54*, 169–175. http://www.sciencedirect.com/science/article/B6V10-47T2GNT-K/2/5e5a42a4855dfd83da36607af3a75b8e.

Park, E.H., Barreto, E., Gluckman, B.J., Schiff, S.J., & So, P. (2005). A model of the effects of applied electric fields on neuronal synchronization. *Journal of Computational Neuroscience*, *19*, 53–70. http://www.springerlink.com/content/w1681302gth46592.

Pinsky, P.F., & Rinzel, J. (1994). Intrinsic and network rhythmogenesis in a reduced traub model for ca3 neurons. *Journal of Computational Neuroscience*, *1*(1–2), 39–60.

Pucihar, G., Miklavcic, D., & Kotnik, T. (2009). A time-dependent numerical model of transmembrane voltage inducement and electroporation of irregularly shaped cells. *IEEE Transactions on Biomedical Engineering*, *56*(5), 1491–1501. doi:10.1109/TBME.2009.2014244.

Radman, T., Su, Y., An, J.H., Parra, L.C., & Bikson, M. (2007). Spike timing amplifies the effect of electric fields on neurons: Implication for endogenous field effects. *The Journal of Neuroscience*, *27*, 3030–3036.

Radman, T., Ramos, R.L., Brumberg, J.C., & Bikson, M. (2009). Role of cortical cell type and morphology in subthreshold and suprathreshold uniform electric field stimulation *in vitro*. *Brain Stimulation*, *2*, 215–228. experimental and Theoretic polarization of neuron.

Reato, D., Rahman, A., Bikson, M., & Parra, L.C. (2010). Low-intensity electrical stimulation affects network dynamics by modulating population rate and spike timing. *The Journal of Neuroscience*, *30*(45), 15,067–15,079. doi:10.1523/JNEUROSCI.2059-10.2010, http://www.jneurosci.org/cgi/content/abstract/30/45/15067.

Richardson, K.A., Gluckman, B.J., Weinstein, S.L., Glosch, C.E., Moon, J.B., Gwinn, R.P., Gale, K., & Schiff, S.J. (2003). *In vivo* modulation of hippocampal epileptiform activity with radial electric fields. *Epilepsia Series 4*, *44*(6), 768–777. http://search.ebscohost.com/login.aspx?direct=true&db=a9h&AN=10130960&site=ehost-live.

Richardson, K.A., Schiff, S.J., & Gluckman, B.J. (2005). Control of traveling waves in the mammalian cortex. *Physical Review Letters*, *94*(2), 028,103. doi:10.1103/PhysRevLett.94.028103, http://prola.aps.org.mutex.gmu.edu/abstract/PRL/v94/i2/e028103.

Sunderam, S., Chernyy, N., Peixoto, N., Mason, J.P., Weinstein, S.L., Schiff, S.J., & Gluckman, B.J. (2009). Seizure entrainment with polarizing low-frequency electric fields in a chronic animal epilepsy model. *Journal of Neural Engineering*, *6*(4). doi:10.1088/1741-2560/6/4/046009. *In vivo* very low freq to modulate excitability in tetanically induced epileptic rats.

Tranchina, D., & Nicholson, C. (1986). A model for the polarization of neurons by extrinsically applied electric fields. *Biophysical Journal*, *50*, 1139–1156.

Traub, R.D., & Milesm, R. (1991). *Neuronal Networks of the Hippocampus*. Cambridge.

Traub, R., Dudek, F., Snow, R., & Knowles, W. (1985a). Computer simulations indicate that electrical field effects contribute to the shape of the epileptiform field potential. *Neuroscience*, *15*(4), 947–958.

Traub, R., Dudek, F., Taylor, C.P., & Knowles, W.D. (1985b). Simulation of hippocampal afterdischarges synchronized by electrical interactions. *Neuroscience*, *14*, 1033–1038.

Traub, R.D., Wong, R.K., Miles, R., & Michelson, H. (1991). A model of a ca3 hippocampal pyramidal neuron incorporating voltage-clamp data on intrinsic conductances. *Journal of Neurophysiology*, *66*(2), 635–650. http://jn.physiology.org/cgi/content/abstract/66/2/635. http://jn.physiology.org/cgi/reprint/66/2/635.pdf.

Vigmond, E., Velazquez, J.L.P., Valiante, T.A., Bardakjian, B.L., & Carlen, P.L. (1997). Mechanisms of electrical coupling between pyramidal cells. *Journal of Neurophysiology*, *78*, 3107–3116.

Weiss, S.A., & Faber, D.S. (2010). Field effects in the cns play functional roles. *Frontiers In Neural Circuits*, 4. doi:10.3389/fncir.2010.00015.

Yi, G.S., Wang, J., Wei, X.L., Tsang, K.M., Chan, W.L., Deng, B., & Han, C.X. (2014). Exploring how extracellular electric field modulates neuron activity through dynamical analysis of a two-compartment neuron model. *Journal of Computational Neuroscience*, *36*(3), 383–399. doi:10.1007/s10827-013-0479-z.